

Fundamentals of Reentry Aerodynamics

Justin Self*

California Polytechnic State University

Reentry flight studies are vital for the design and analysis of human and sample return space missions, to name a few recent examples. The atmospheric reentry problem involves the entire orbital and flight mechanics regime, atmospheric composition and aerothermal chemistry, and hypersonic boundary layer and shock characteristics. This review summarizes the fundamentals of a theoretical spaceflight mission that starts at a 320 km circular orbit, then performs an impulsive maneuver (total $\Delta v = 3.05$ km/s) translunar injection (TLI) to take a free-return trajectory around the Moon and ultimately reenters Earth's atmosphere after about 166 hours. Reentry velocity and flight path angle are 11 km/s and -23.7° , respectively. The flight reentry corridor is simulated with variation in ballistic coefficient to model tumbling or breakup during reentry. It was found that a deployable heat shield that doubles the effective drag coefficient reduces splashdown velocity by 9.25% over a heat shield with a 10% increase in drag coefficient. Ground footprints were plotted and compared across varying flight path angles. The chemical equilibrium calculator developed for this work produced plots that agree reasonably well with published values for most of the atmospheric gas species considered. Vibrational excitation, oxygen and nitrogen dissociation, and ionization of common gas species in earth's atmosphere were simulated and plotted with the reentry flight envelope altitude and velocity map. Results from all simulations agreed reasonably well with literature. Stagnation temperatures and pressure plots were developed and agreed with literature values. Finally, computational fluid dynamics (CFD) models were developed that simulated the sphere in various subsonic and supersonic steady and unsteady flow regimes; pressure and velocity contours are presented and agree with existing literature results.

I. Nomenclature

A	=	Reference area of spacecraft
a	=	Speed of sound
C_D	=	drag coefficient
f	=	change factor for ballistic coefficient variation
F_D	=	drag force
g	=	gravitational constant
h	=	orbital angular momentum
i	=	orbital inclination
TA	=	orbital true anomaly
ΔH_f^0	=	heat of formation at standard atmosphere and pressure
K	=	Kelvin
kp	=	equilibrium constant
m	=	mass of spacecraft
M	=	Mach number
P	=	static pressure
P_t	=	total pressure
Q	=	heat flux
Q'	=	partition function
\vec{r}	=	spacecraft position vector
r	=	spacecraft position vector, normalized
\ddot{i}	=	acceleration of spacecraft in orbit

*AERO 407 | Reentry Aerodynamics, Winter 2024. Dr. Nandeesh Hiremath, Department of Aerospace Engineering

S	=	reference area
T	=	static temperature
T_t	=	total temperature
\vec{v}	=	spacecraft velocity vector
v	=	spacecraft velocity vector, normalized
V_c	=	tangential velocity of spacecraft orbit
W	=	spacecraft weight

Greek symbols

α_0	=	Right ascension at translunar injection
β	=	ballistic coefficient
η	=	transformed coordinate component, boundary layer theory
γ	=	flight path angle
Ω	=	Right Ascension of the Ascending Node
ω	=	argument of perigee
λ	=	lunar arrival angle
μ_e	=	gravitational parameter, earth
μ_m	=	gravitational parameter, moon
ρ	=	density
θ	=	characteristic temperature, vibrational excitation mode
ξ	=	transformed coordinate component, boundary layer theory

Acronyms

ECI	=	Earth-Centered Inertial frame
KE	=	kinetic energy
LEO	=	Low Earth Orbit
$LVLH$	=	Local-Vertical-Local-Horizontal (body) frame
RSW	=	RSW frame (LVLH or body frame)
SOI	=	Sphere of Influence
TLI	=	TransLunar Injection

II. Introduction

REENTRY aerodynamics is a vital component of the spaceflight mission systems in today's world. From John Glenn's successful reentry in 1962 (the first ever) to the commonplace return of astronauts and cosmonauts from the International Space Station, missions that are designed to survive the extreme atmospheric reentry environment are carefully analyzed and studied before they are put into motion. The primary focus of this review is to characterize the basic principles of high-speed aerodynamics, typically in the hypersonic velocity regime, from the perspective of a lunar survey mission capsule during its orbital flight and safe reentry into Earth's atmosphere. The topics covered in this review include a lunar free-return trajectory simulation, reentry flight mechanics into the upper atmosphere and flight trajectory for varying flight path angles and ballistic orientations, aerothermal chemistry for the upper atmosphere during hypersonic reentry, hypersonic boundary layer theory, and several CFD simulations for super- and subsonic flight modes.

A. Lunar Free-Return Trajectory and Reentry Mechanics

The hypothetical mission begins with an Apollo 11-sized spacecraft in a circular orbit around Earth. The spacecraft then performs an instantaneous impulsive-thrust maneuver into a transfer trajectory that will take the spacecraft on a flyby of the moon with no further engine burn required. The gravitational dynamics of the system assure the rest of the flight trajectory; namely, that the spacecraft will fly by the moon and then return to the earth for a splashdown. Once the spacecraft has reached 100 km altitude, it is considered to have re-entered the earth's atmosphere and atmospheric flight dynamics take over. Details of the mission parameters and simulation are given in Section III.A.

Next, a flight reentry envelope is simulated for varying reentry flight path angles, varying ballistic coefficients (simulating a tumbling spacecraft or one that is breaking up), and finally, how the ground-track and flight trajectory would change if a hypothetical umbrella-like heat shield were to be deployed at varying altitudes.

B. Chemical Equilibrium and Aerothermochemistry

This topic started with a cursory understanding of what is known as the “thermal barrier” and how engineers learned how to overcome it for realistic reentry systems. Originally, the major concern of reentry was to find a way to survive the aerodynamic heating. Many researchers thought it would be impossible and coined the term “thermal barrier”; similar to how previous researchers believed that supersonic flight was impossible [1]. An example of why this fear existed can be apprehended by considering the following (taken from [1]):

$$KE = \frac{1}{2}mv^2 \quad (1)$$

where m is the mass of the satellite and v is its velocity. During reentry, all this kinetic energy must be dissipated and converted into heat to decelerate the spacecraft to zero velocity.

$$Q = KE = \frac{1}{2} \frac{W}{g} v^2$$

where Q is the dissipated heat and W is the satellite weight, and g is the gravitational constant. For a circular orbit,

$$v = 26,000 \text{ ft/s}$$

the aerodynamic heating thus would be:

$$\frac{Q}{W} = \frac{v^2}{2g} = 13,500 \left[\frac{\text{Btu}}{\text{lb}} \right]$$

If all the KE went into heating the object, almost no material on earth would survive the process. For example, tungsten’s vaporization energy is 1,870 Btu/lb. Clearly it seems that there is a problem; there may indeed be a “thermal barrier”.

But the reality is, as researchers found out, not all of the kinetic energy goes into heating the material. Indeed, much of (in fact, most) the energy goes into heating the fluid around the reentry spacecraft, which leads to an interesting study of aerothermal chemistry, chemical dissociation, and ionization of air particles around a reentry vehicle. This was one of the primary takeaways from this learning module, and, in fact, this is an extremely useful concept to understand when analyzing or designing reentry systems. Various aerothermal interactions between a spacecraft and earth’s atmosphere is the subject of our analysis in Sections III.B and IV.B.

C. Stagnation Pressure and Temperature

The heating rate at the stagnation region is a good starting place for a basic understanding of reentry heating systems, since many simplifying assumptions can be made; the very front portion of a sphere, for instance, can respect only the normal shock component of the bow shock and can assume isentropic flow from the streamline between the shock and boundary layer [1]. This section focused on the characteristics of hypersonic boundary layer equations that were derived from the Navier-Stokes equations. Velocity and temperature profiles in both Cartesian and transformed ξ, η coordinate systems were analyzed for self-similarity and computational efficiency. The main takeaway of this section was to understand the viscous-dominated regions of the flow very near the wall (or surface) of the spacecraft during reentry. The plot developed in Section IV.C considers only vibrational excitation energy and, consequently, the reported stagnation temperatures are very high. If atomic dissociation and ionization energy modes were added to this model, the stagnation temperature *as seen by the spacecraft structure* would decrease.

D. Computational Fluid Dynamics of a Sphere

Finally, CFD simulations were performed on a sphere passing through the atmosphere at various flight speeds in steady and unsteady flow cases. Results from these computations are given in Section IV.D.

III. Methodology

A. Lunar Free-Return Trajectory and Reentry Mechanics

1. Lunar Free-Return Trajectory

In this model, several simplifying assumptions were made. Namely, (i) orbital motion was computed assuming a simple two-body motion system (i.e., spacecraft + Earth or spacecraft + Moon); (ii) all bodies lie in the same plane; (iii) orbital perturbations are ignored; (iv) the moon is in a circular orbit around Earth. A more robust model would consider the more realistic situations in which bodies are out of plane and orbital perturbations are accounted for.

All orbit propagation was performed numerically using the MATLAB ode45 ordinary differential equation solver to solve the equations of two-body orbital motion given in Eqn. 2. Two-body motion was chosen for simplicity and is adequate to show the general concept of a lunar flyby and free-return trajectory.

The two-body orbital motion equation used is:

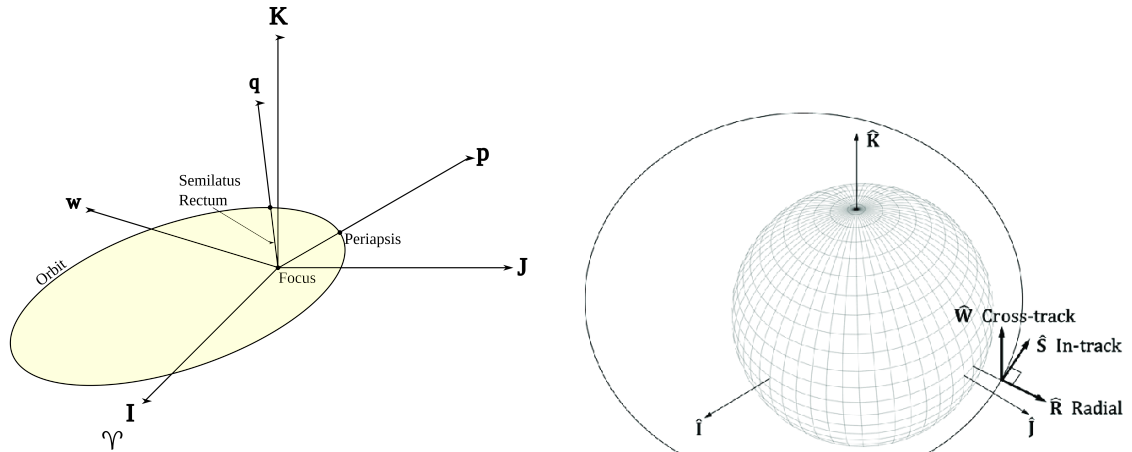
$$\ddot{\vec{r}} = -\frac{\mu}{r^3}\vec{r} \quad (2)$$

where

- $\ddot{\vec{r}}$ = is the spacecraft acceleration due to gravity around the main body
- μ = gravitational parameter of the main body; $\mu_e = 398600 \text{ km}^3/\text{s}$; $\mu_m = 4902.8 \text{ km}^3/\text{s}$
- r = magnitude of the orbital position vector

For most of the mission, the spacecraft is under the primary gravitational influence of the earth (neglecting the sun). Common orbital elements (angular momentum, h , eccentricity, e , inclination, i , right ascension of ascending node, Ω , argument of perigee, ω , and true anomaly, θ), typically given in orbital frame (or *perifocal*, shown in Fig. 1a), are described here in Earth-Centered-Inertial (ECI). Spacecraft orientation at any point during the orbit is in the Local-Vertical-Local-Horizontal (LVLH) or *RSW* frame (see Fig. 1b). When the spacecraft enters the moon's sphere of influence (SOI), the primary gravitational body in our model is the moon (see Fig. 6a).

See Section III.A for the simulation results.



(a) Orbital (perifocal) reference frame describing the orbit of the spacecraft. For simplicity, in this problem the orbital plane is in the same plane as the ECI plane. Image courtesy of [2].

(b) ECI frame and LVLH (also known as the RSW) frame used in this work. The spacecraft body frame is synonymous with the RSW frame. Image courtesy of [3].

Fig. 1 Definitions of the orbital frame (perifocal) and LVLH frames. The ECI frame is shown as \hat{i} , \hat{j} , and \hat{k} , unit vectors in both figures.

2. Flight Mechanics

For this problem, we began by making the following assumptions:

- 1) All motion is in the xy plane, where x is an inertial horizontal axis representing the downrange distance and y is an inertial vertical axis representing altitude (see Fig. 2).
- 2) The reentry capsule is treated as a non-lifting body
- 3) Earth's radius at all points during the mission is equal to the equatorial radius: $R_e = 6378$ km
- 4) The characteristic area normal to the flow during the entire reentry trajectory is assumed to be circular in both the x and y directions. That is, the Apollo 6 command module is geometrically modelled as a sphere of the same diameter as the command module's actual largest diameter.

Ballistic coefficient, defined in Eqn. 3, was computed using literature values for the Apollo 6 command module, where W is spacecraft weight, C_D is the average drag coefficient over the flight regime, and S is the characteristic area in the ram-facing direction during reentry.

$$\beta = \frac{W}{C_D S} \quad (3)$$

Acceleration due to gravity is permitted to change as a function of altitude according to Eqn. 4.

$$g_h = g_0 \left(\frac{R_e}{R_e + h} \right)^2 \quad (4)$$

where

g_0 = Acceleration due to gravity at earth's surface

R_e = Radius of the earth

h = Altitude

Flight path angle, γ , is permitted to change during descent. Acceleration in the x and y directions are computed numerically using MATLAB ode45 ODE solver using Eqns. 5, 6, and 7 (from [1]).

$$\dot{V} = -g_h \left[\frac{D}{L} \frac{L}{W} + \sin\gamma \right] \quad (5)$$

$$\dot{\gamma} = \frac{g_h}{V} \left[\frac{L}{W} - \left(1 - \frac{V^2}{V_c^2} \right) \cos\gamma \right] \quad (6)$$

$$\dot{h} = V \sin\gamma \quad (7)$$

where

D = Drag force

L = Lift force

W = Weight of spacecraft

γ = Flight path angle

V = Magnitude of velocity

V_c = Tangential velocity of an osculating (normal) orbit if the spacecraft were in earth-bound orbit at a given altitude, given in Eqn. 8.

$$V_c = \sqrt{g_h R} \quad (8)$$

Where R is the altitude plus radius of the earth at any moment. This is equivalent to the familiar tangential velocity of a body in circular motion.

See Section IV.A for the simulation results.

B. Chemical Equilibrium and Aerothermochemistry

A chemical equilibrium calculator was developed in MATLAB.* The program takes only temperature (as an array or a single value) and a species ID, which allows the user to choose which gas species to analyze (of the seven coded up). Earth's atmosphere consists of gases made from the basic elements of nitrogen (~ 79%) and oxygen (~ 21%), with other trace elements. This gives out the possibility of several combinations of N and O resulting in chemical equilibrium

*See Appendix A for outputs from the calculator and associate validation methods; the calculator agrees mostly well with published values for common gas species.

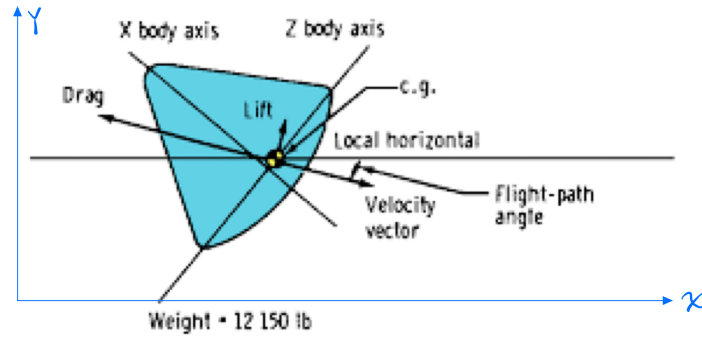


Fig. 2 Free body diagram of a reentry capsule (in our case, the Apollo 6 command module). We treat the capsule as completely ballistic, that is, there is no lift component. The x and y coordinates shown here are in an inertial frame not fixed to the spacecraft and are the same as in Figs. 8-10.

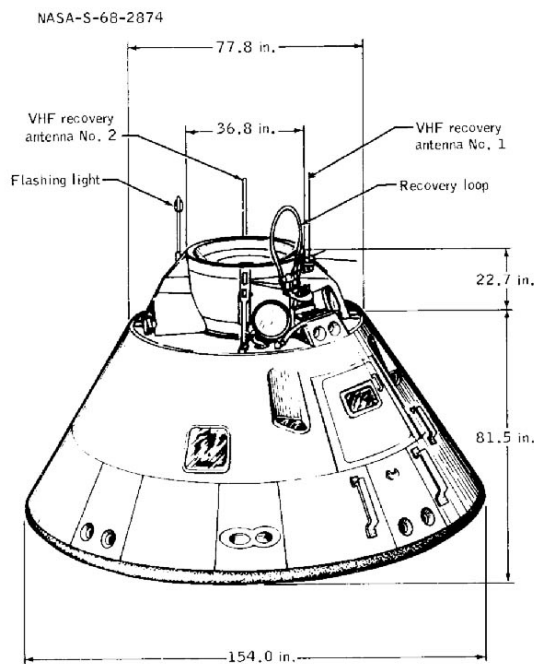


Figure 1-9. - Apollo command module (CM) after landing

Fig. 3 Apollo 6 command module dimensions used to determine drag coefficient in our study. [4].

mixtures present to equilibrium temperature and pressure (or enthalpy), namely, N_2 , O_2 , N , O , NO , NO_2 , NO^+ , e^- . Equilibrium mixture properties, enthalpy of the mixture, and real gas constant of the mixture for a given equilibrium temperature and pressure was computed. Results from the analysis are given in Section IV.B.

Additionally, a flow chart explaining the steps/procedures used in calculating the equilibrium mixture was developed and is included in the Results section. Mole fraction vs. temperature was computed for all seven species above at 1, 0.1, and 0.01 atmospheric pressures (atms). Results were validated (as much as possible) using JANAF tables or NASA literature results.

C. Stagnation Pressure and Temperature

The Mach/Altitude profile for a spacecraft during reentry was calculated using thermally perfect gas equations by accounting for the vibrational modes under thermal equilibrium conditions. Real gas effects and non-equilibrium chemical kinetics at high-altitude hypersonic conditions are beyond the scope of this work. Speed of sound becomes:

$$a^2 = RT \left(1 + \frac{\gamma_{perf} - 1}{1 + (\gamma_{perf} - 1) \left(\frac{\theta}{T} \right)^2 \frac{\exp^{\theta T}}{(\exp^{\theta T} - 1)^2}} \right) \quad (9)$$

Where a is the speed of sound, γ is a function of static temperature, T , the characteristic vibrational mode temperature for air $\theta = 3056\text{K}$, and R is the real gas constant for air.

Isentropic relations in freestream conditions were used to obtain the total pressure and temperature at a given altitude as shown in Eqns. (10) and (11). Stagnation pressures *at the front* of the deorbiting spacecraft, shown in Figure 18, were found by solving normal shock relations corrected for vibrational modes.

$$\frac{P}{P_t} = \left(\frac{T}{T_t} \right)^{\frac{\gamma}{\gamma-1}} \quad (10)$$

$$\frac{T}{T_t} = \left(1 + \frac{\gamma-1}{2} M^2 \right)^{-1} \quad (11)$$

$$\frac{P_{t_1}}{P_{t_0}} = \left(\frac{(\gamma+1) M^2}{(\gamma-1) M^2 + 2} \right)^{\frac{\gamma}{\gamma-1}} \left(\frac{\gamma+1}{2\gamma M^2 - (\gamma-1)} \right)^{\frac{1}{\gamma-1}} \quad (12)$$

Figure 18 indicates that the spacecraft approaches the subsonic region around 70 km, and it is assumed that conditions after the subsonic regime are constant—or the spacecraft has burned up. The latter is more likely since very high aerodynamic heating loads on the spacecraft occur between 70 km and 75 km altitude.

D. Computational Fluid Dynamics of a Sphere

This batch of simulations fall into four general categories: subsonic flight with steady and unsteady flow (2 cases), and supersonic flight for steady and unsteady flow (2 cases). All simulations were run with an aluminum sphere of 25 mm radius. The fluid medium is air at standard temperature and pressure with ideal gas assumption. All simulations were conducted in *Ansys Fluent 2024 Student Edition*. The methodology for this section involved the characterization of the desired flight regimes, transforming them into input parameters, and comparing the results with literature values. See Section IV.D for CFD results.

IV. Results and Discussion

A. Lunar Free-Return Trajectory and Reentry Mechanics

1. Lunar Free-Return Trajectory Results

This mission begins with a spacecraft in a 320 km circular parking orbit just before performing an impulsive (instantaneous) thrust maneuver (called the Translunar Injection, or TLI) that will result in a *free return trajectory* around the Moon and back. A *free return trajectory* is a trajectory in which a single burn is performed and the remainder of the flight trajectory is a result of the gravitational dynamics of the bodies themselves.

Following the ‘Coplanar Patched Conic Lunar Trajectories’ example in Curtis [5], we begin with the following mission parameters: right ascension at TLI, α_0 , is 28° , flight path angle, γ , is 6° , and the lunar arrival angle, λ , is 55° (see Fig. 4). The full mission trajectory is shown in Fig. 5 and mission parameters are given in Table 1.

After departing low earth orbit (LEO), the spacecraft travels on an elliptical trajectory toward the Moon. The point at which the spacecraft encounters the Moon’s gravitational sphere of influence (SOI) is known as the *patch point*. Once the spacecraft enters the Moon’s SOI (ignoring perturbations) the Moon becomes the only body under which gravitational motion takes place.

During the lunar flyby, the spacecraft travels within 1021.7 km of the surface at *perilune*; the closest approach in the orbit. This lunar flyby, as seen from a lunar-fixed frame, is shown in Fig. 6a.

After the roughly 35-hour long lunar flyby, the spacecraft exits the Moon's SOI and follows an elliptical path back to Earth. In this model, the TLI burn was sufficient to produce this trajectory, but the velocity at which the spacecraft crosses the original parking orbit is too high to sustain a LEO orbit, and the spacecraft crashes into Earth's atmosphere. The following vectors give the position and velocity upon reentry, or, the moment the spacecraft altitude crosses the 100 km atmospheric threshold.

$$\vec{r} = \begin{bmatrix} -5931.2 \\ 2604.8 \\ 0 \end{bmatrix} \text{ km}$$

$$\vec{v} = \begin{bmatrix} -1.8489 \\ -10.850 \\ 0 \end{bmatrix} \text{ km/s}$$

The magnitudes of these reentry parameters are:

$$r = 6478 \text{ km (100 km altitude)}$$

$$v = 11.007 \text{ km/s}$$

Flight path angle for this reentry is

$$\gamma = -23.7^\circ$$

with respect to the local horizon, which we will use as an input for the next section. Fig. 4, from [5], shows the first part of the lunar trajectory in the ECI frame. Compare this to our simulation in Fig. 5, which shows (in ECI) the full lunar mission (except the flyby itself). Table 1 gives the highlights of the mission broken down by mission phase. Note that the Δv for the TLI burn was a manageable 3.0526 km/s, and the full mission time was just under one week.

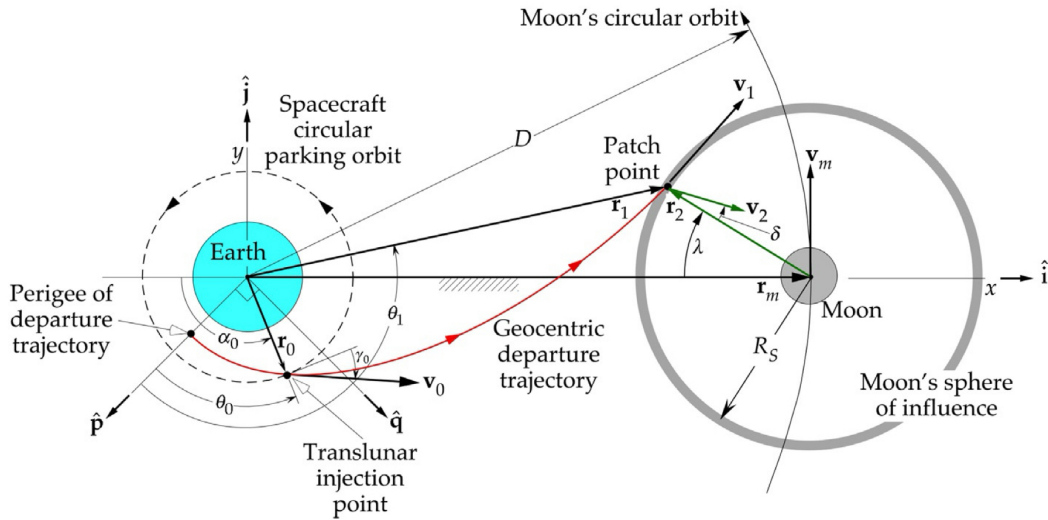


Fig. 4 Fig. 9.2 from [5] showing a coplanar lunar trajectory from Earth to the Moon SOI. Shown with a nonrotating Earth-Centered Inertial (ECI) frame (x and y -axes). Not to scale.

Table 1 Lunar flyby mission timeline and Δv values

Mission Phase	Mission elapsed time	Δv [km/s]
Translunar Injection (TLI)	0	3.0526
Transfer to Moon SOI	66.4545 h	0
Arrival at perilune	83.9867 h	0
Depart Moon SOI	101.5190 h	0
Reentry at 100 km	166.5107 h	0

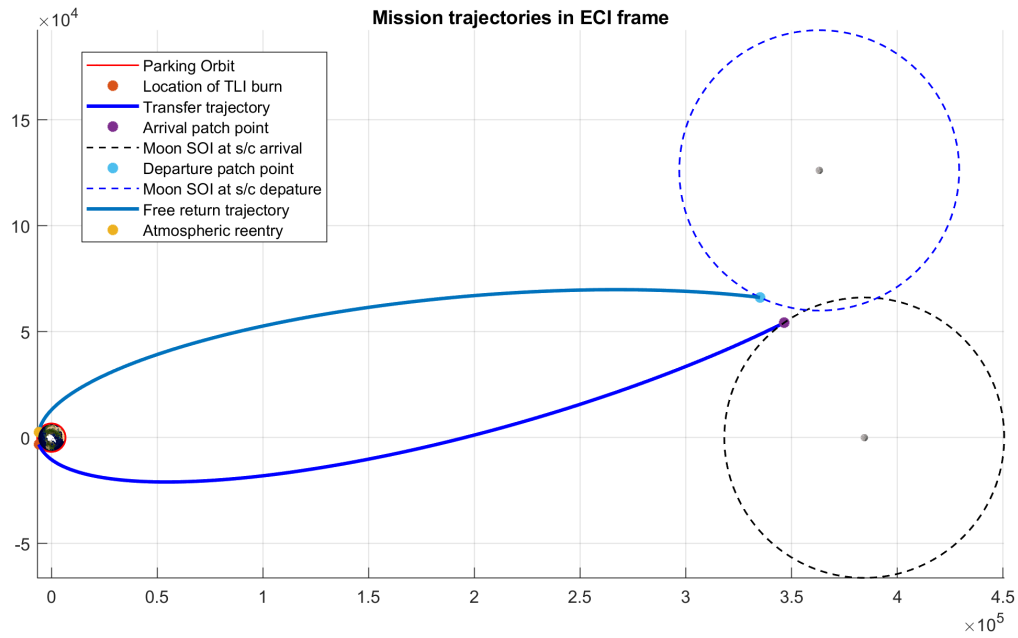
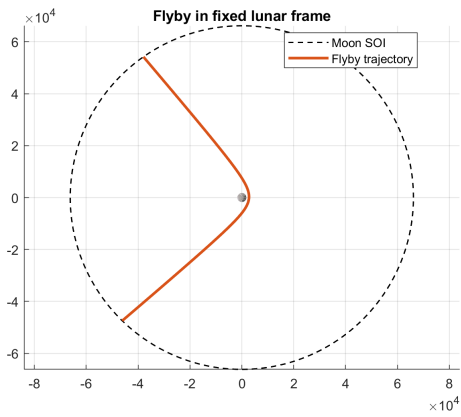
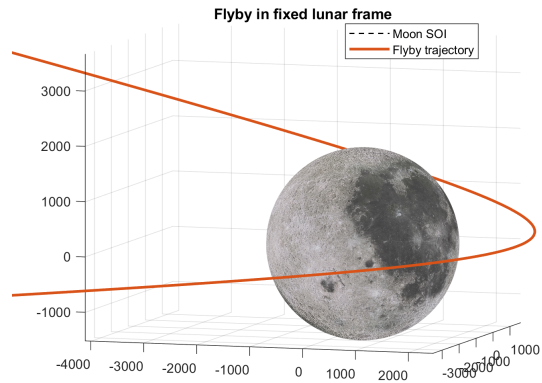


Fig. 5 Full lunar flyby trajectory from the non-rotating ECI frame. The moon and its SOI are shown at various positions during the flight. The bottom moon and SOI represent the moon’s position when the spacecraft arrives at the patch point for entry into the lunar system. The top moon and SOI represent the moon’s position when the spacecraft departs the SOI at the patch point on the return trajectory. The lunar flyby is not shown in ECI here, but is shown in Fig. 6a for clarity. A closer view of the earth parking orbit and reentry angle is depicted in 7.



(a) Lunar flyby as seen from an inertial lunar frame. The spacecraft enters the moon's SOI on the top, flying in a clockwise manner.



(b) Lunar flyby. Perilune (closest approach) altitude is 1021.7 km and occurs about 84 hours into the mission.

Fig. 6 Lunar flyby in fixed lunar frame.

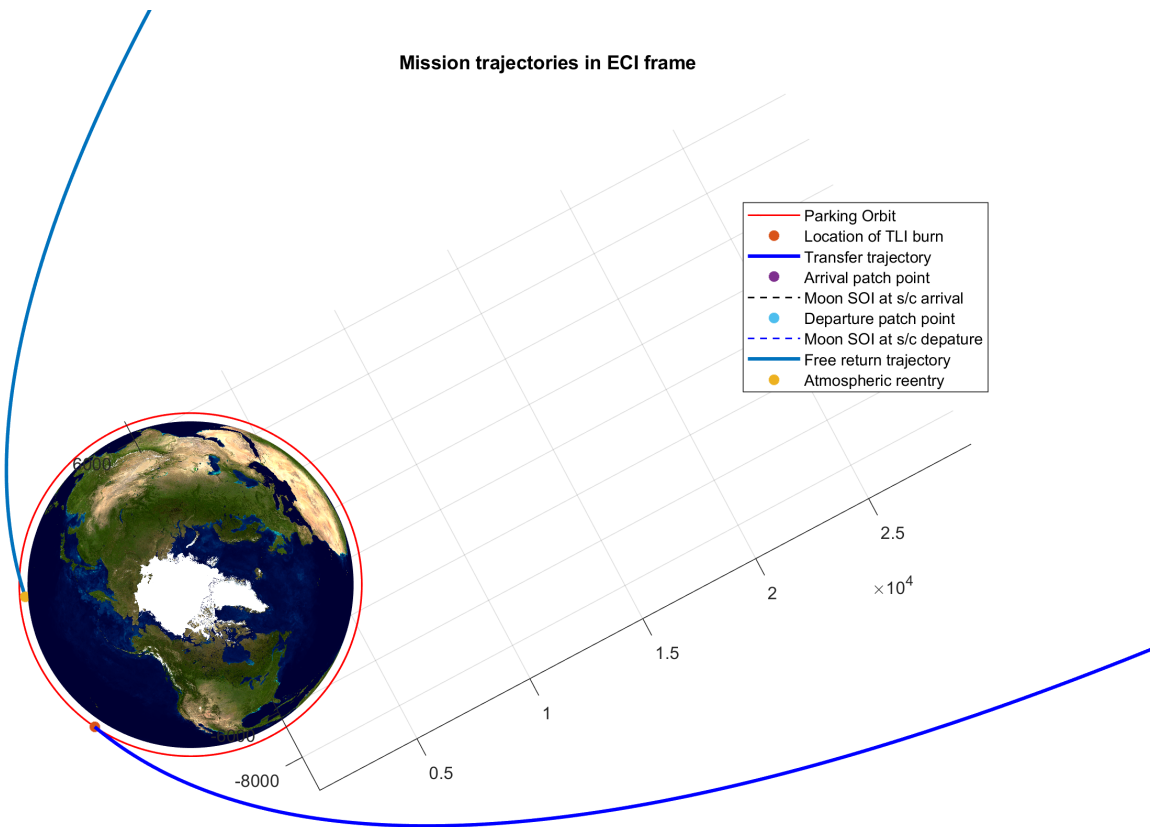


Fig. 7 TLI and reentry shown in the ECI frame. The parking orbit and TLI position, both in red, shows the starting position for the mission. The lunar transfer trajectory is shown in dark blue (bottom of this image), while the return trajectory is shown in light blue (top). Only one burn at TLI is required to perform the entire trajectory. The spacecraft reenters Earth's atmosphere at the location shown in orange.

2. Flight Mechanics Results

Varying Ballistic Coefficient

Ballistic coefficient, defined in Eqn. 3, was varied from 0.1β to β (in increments of 0.10) to roughly model tumbling or spacecraft breakup during reentry. Simulation results showing the altitude vs. velocity trajectory with ten different values for the ballistic coefficient are plotted in Fig. 8.

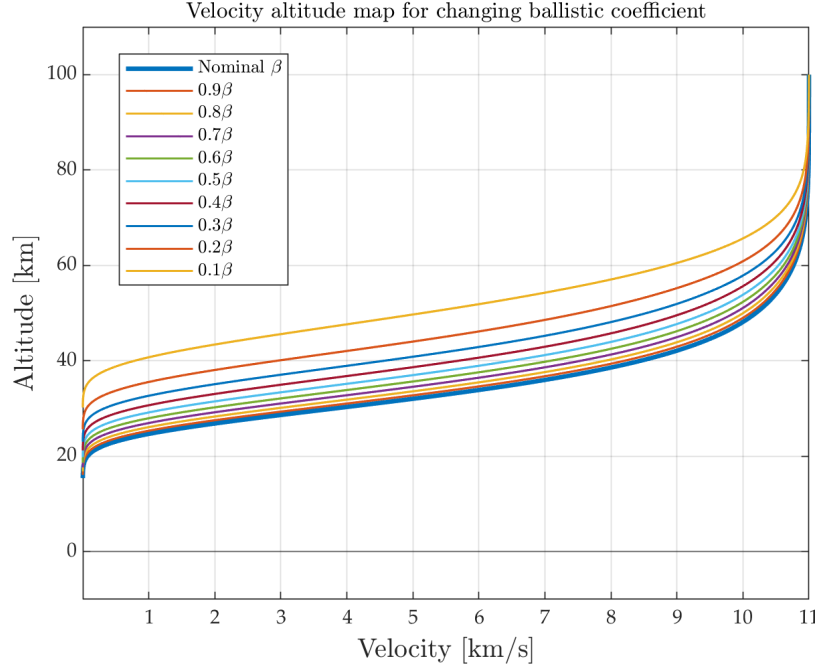


Fig. 8 Flight reentry corridor with various inputs for the ballistic coefficient. Varying β roughly models a spacecraft tumbling or breaking up on the way down.

Varying Flight Path Angle

As an object encounters earth's atmosphere at an initial flight path angle γ , there are three options designers can take depending on mission objectives. First, γ can be reduced to a very small angle and the spacecraft will skip across the atmosphere much like a rock skips across the surface of a pond. This is known as *aerobraking* and is an effective method for reducing velocity on the way into the atmosphere for a soft surface landing or as a way to change the orbital altitude and velocity of an object without using Δv .

Next, the flight path angle could be increased to such a steep angle that the object encounters the full brunt of the atmospheric heating and friction at hypersonic reentry velocities, inevitably leading to burn up. Third, if γ is just the right angle, the object can reenter the planetary atmosphere without skipping off *or* burning up. This is what the Apollo engineers worked out, since their precious payload was three astronauts who needed to survive the experience.

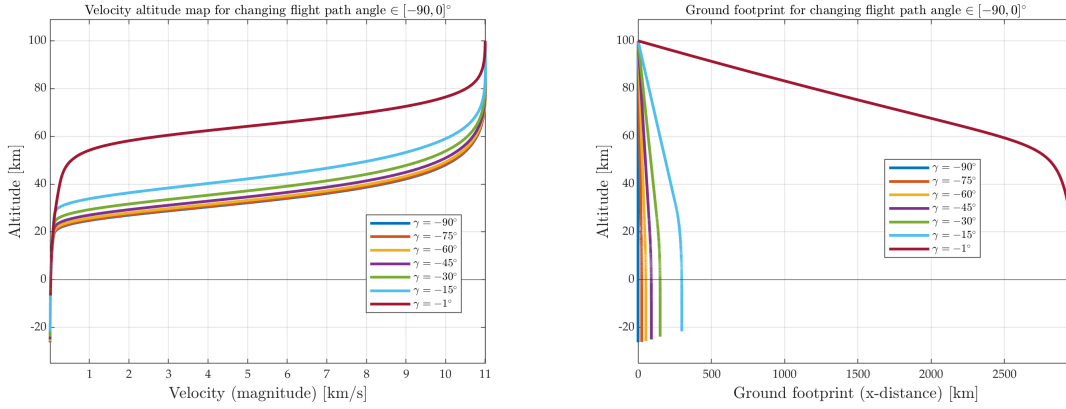
Fig. 9 shows how different *initial* flight path angles affect the reentry flight corridor. As a result of Eqn. 6, the flight path angles do not remain constant during the process, which makes sense for a real system with drag forces acting in (in this case) two dimensions. Note that when $\gamma = 0$, the spacecraft stays in circular orbit at 100 km since orbital perturbations and (importantly) atmospheric drag, are not considered.

Heat Shield Deployment

The final task in this deliverable is to simulate a heat shield being deployed instantaneously during reentry. The heat shield is modelled as a change in drag coefficient by some percent of the original C_D value by rearranging the equations for drag force, F_D , and β , ballistic coefficient.

$$F_D = \frac{1}{2} \rho v^2 C_D S \quad (13)$$

$$\beta = \frac{m}{C_D S} \quad (14)$$



(a) Velocity-altitude map with fixed ballistic coefficient with varying flight path angles, γ . (b) Ground footprint (x -distance vs. altitude) of the spacecraft for varying initial reentry flight path angles.

Fig. 9 Flight reentry corridor as seen from an inertial frame showing (a) velocity and altitude and (b) ground footprint as the spacecraft reenters the earth's atmosphere. Note that for shallow entry flight path angles, $\sim 1^\circ$, the spacecraft essentially skips off the atmosphere. This plot does not consider the curvature of the earth, but simply shows the elongation in x -distance as a result of different γ angles.

Where

- ρ = Density of atmosphere, where $\rho = \rho(\text{altitude})$
- v = Magnitude of freestream velocity
- C_D = Drag coefficient
- S = Characteristic ram-facing cross-sectional area
- m = Mass of the spacecraft

Thus, a change in C_D in terms of the quantities already defined is by multiplying C_D by the desired change factor:

$$\beta_1 = \beta f^{-1}$$

Where

- β = Nominal drag coefficient
- f = Change factor, i.e., 1.1 for an increase of 10%

Simulation altitudes for heat shield deployment are 80 km, 60 km, and 40 km. The percent changes in drag coefficient were 10%, 50%, and 100%. Eqns. 5 - 7 were integrated for 2000 seconds, which proved to be too long. 500 seconds proved to be enough to see the flight trajectory.

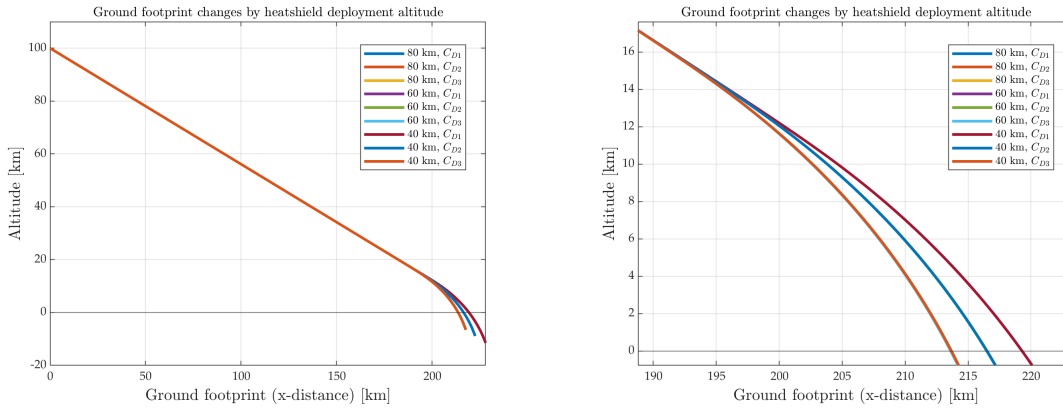
If one were interested in truly slowing down a capsule with human occupants, additional braking would be required to achieve the program's design splashdown speed of 9.5 - 11 m/s (values from [6]). The impact velocities for the three C_D configurations are shown in Table 2. Notice that when the drag coefficient is doubled, the impact velocity is reduced by 9.25% over the $1.1C_D$ case.

Table 2 Impact velocities by Heatshield Configuration

Heatshield Configuration	Impact velocity [m/s]
$1.1C_D$	54.3
$1.5C_D$	51.7
$2C_D$	49.5

Slower, but not slow enough for human cargo. The full ground footprint is shown in Fig. 10 from 100 km and zoomed in for clarity. Notice that the major characteristic is the change in drag coefficient, not deployment altitude. This is thought to be due to the drag coefficient not being increased enough through the heatshield deployment, which, if

increased to model parachute deployment, may show a more radical braking profile at higher altitudes, and a more tolerable landing speed.

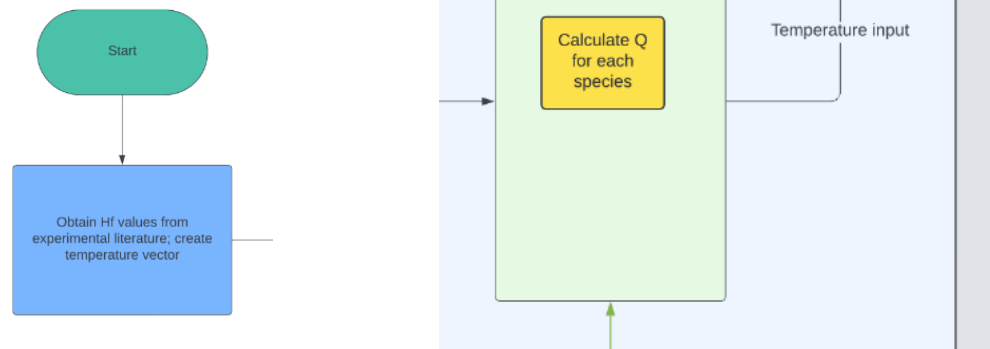


(a) Different deployment altitudes had no significant effect on ground footprint or impact velocity. Effects due to the change in drag coefficient dominated. (b) Zoomed-in version of (a), showing the difference between heat shield configurations. Deployment altitude was not a significant parameter in this study.

Fig. 10 Heat shield deployment at 80, 60, and 40 km altitude with three drag coefficient configurations.

B. Chemical Equilibrium and Aerothermochemistry Results

A basic flowchart that follows the MATLAB script used to develop the equilibrium plots here is shown in Fig. 39. For clarity, each subsection of the flowchart is given in smaller packages in Figs. 11a 14, with brief explanations in the captions.



(a) First, heat of formation at standard temperature and pressure (ΔH_f^0) values are obtained from literature for each gas species under consideration. (b) The partition function, Q' , is calculated next in a small loop. The algorithm for this loop is shown in Fig. 12.

Fig. 11 First two steps of aerothermal calculator algorithm. A temperature array must be created at this point for the code to loop through. The rest of the flowchart is inside a large loop that runs through each temperature value in the array. In this study, the temperature array was 100 points in [2000,6000] Kelvin.

For the full algorithm flow chart in one place, see the Appendix B.

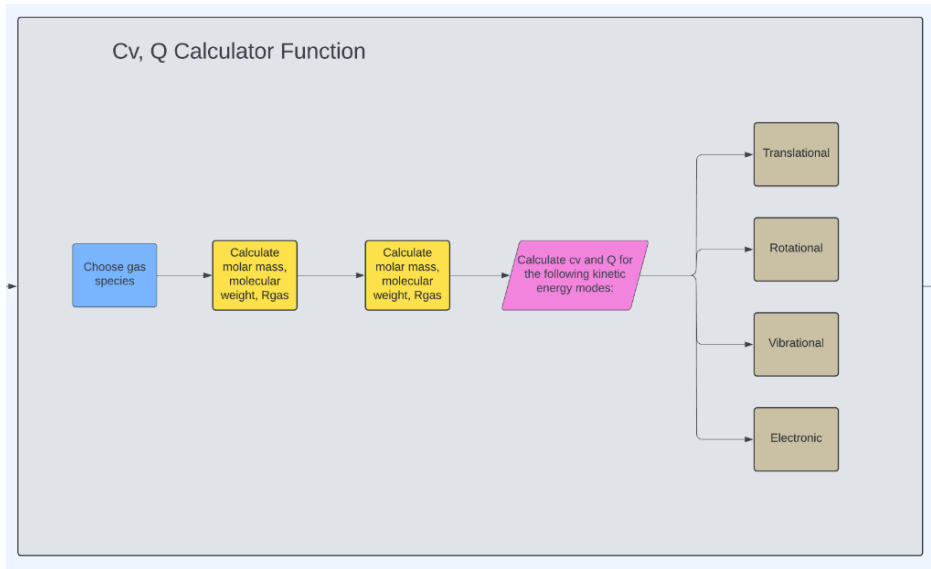


Fig. 12 The partition function and c_v calculator loop, which takes only temperature as an input. The outputs are Q for one gas species at the given temperature value, $T(i)$.

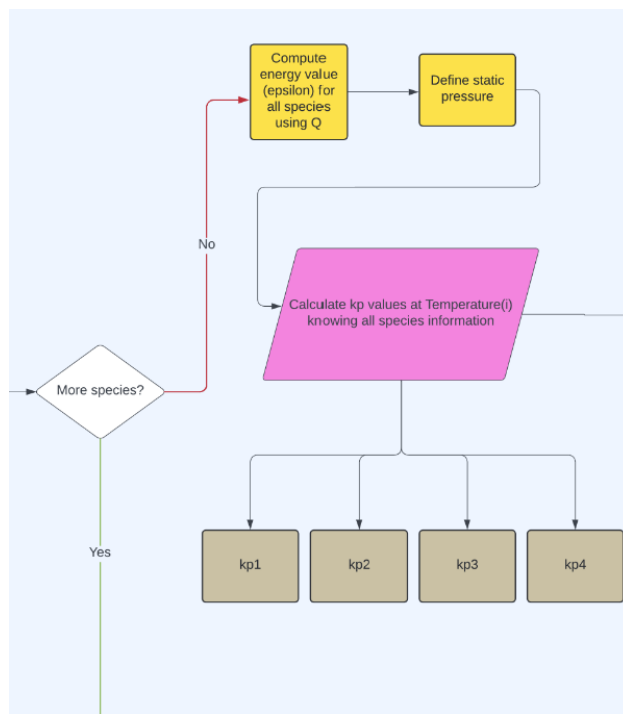


Fig. 13 The Q loop is repeated until a Q value for each gas species has been obtained. In this study, seven gas species were studied. Once all species have a Q value (at the same $T(i)$), energy values are calculated, static pressure is defined, and kp values are computed.

The function inputted into the `fsolve` function is below. Note the sensitivity of the initial guesses. These guesses produced reasonable plots, shown in Figs. 15b - 16b.

```

%..... Call fsolve function
% NOMENCLATURE:
  
```

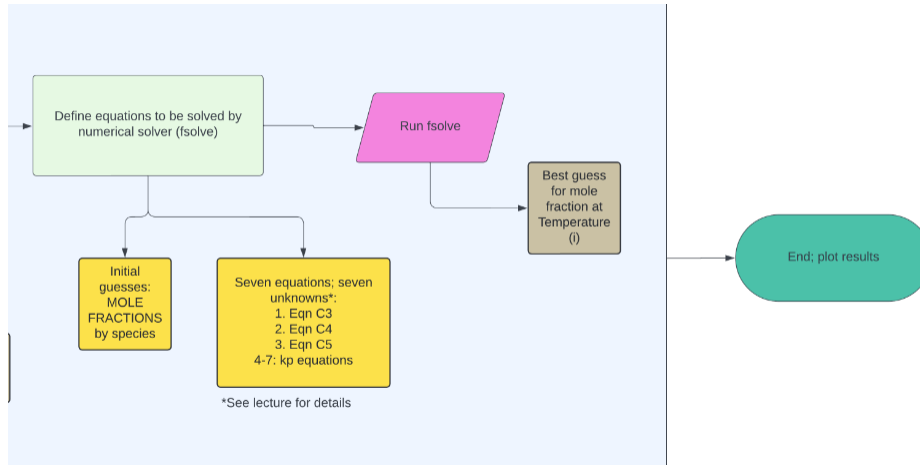


Fig. 14 This part of the algorithm takes the computed parameters and calculates the mole fraction for each species given an initial guess. The solver function is given below in the text. This whole process is repeated through every element in the temperature array, $T(i)$, and final outputs are plotted.

```

%1:N, 2:N2, 3:NO, 4:NO+, 5:O, 6:O2, 7:e-
f = @(x) [((x(1) + 2*x(2) + x(3) + x(4))/(x(5) + 2*x(6) + x(3) + x(4)))
- 0.79/0.21;
x(4) - x(7) ;
x(1) + x(2) + x(3) + x(4) + x(5) + x(6) + x(7) - 1;
kp1 - (((x(5)^2)/(x(6))))*P;
kp2 - (((x(1)^2)/(x(2))))*P;
kp3 - (((x(1)*x(5))/(x(3))))*P;
kp4 - (((x(4)*x(7))/(x(3))))*P;
guess = [0.7,0.1,1e-5,1e-5,0.2,1e-5,1e-5]; % final values on given plot
x(i,1:7) = fsolve(f,guess);
  
```

Mole Fraction vs. Temperature

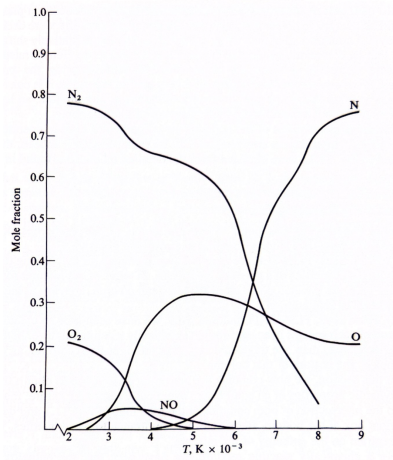
Obtaining the mole fraction vs. temperature plot given by [7] was not trivial and required the simultaneous solving of seven nonlinear equations. We attempted to use MATLAB's native `fsolve` nonlinear equation solver, shown in Figs. 15b, 16a, and 16b. Although the trends are not exactly in agreement as in Fig. 15a, the general trends of each species do agree reasonably well with the known trends.

For instance, Anderson ([7]) shows that N_2 should start around 0.79% mole fraction at around 2000K, then drop off as temperature increases (at 1 atm). Fig. 15b generally follows this trend, starting at 0.79 and slowly decreasing with a bump around 4000K, then decreasing rapidly afterwards. Monatomic nitrogen, N , steadily increases around 4000K, which is also reflected in Fig. 15b. Atomic oxygen, O , increases and peaks around 5000K, then decreases. Our model shows this peak around 3500K, but the species decreases after that. In both cases, O_2 mole fraction decreases rapidly, and NO is very small but peaks in the lower temperature regions.

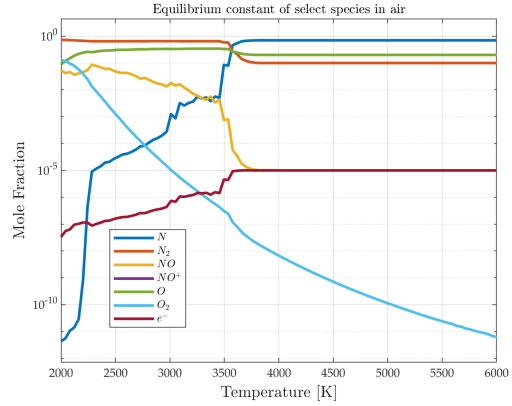
Unfortunately, the solver did not close for many of the iterations and the numerical results are not ideal. This is thought to be an artifact of the electronic energy values being subject to disagreement with Anderson's values, since the values used in our model were largely derived from the JANAF tables ([8]) and, in many cases, only the first few degeneracy states were considered. It is possible the characteristic electronic temperature used in the equations differed from Anderson's as well, which would yield vastly different results.

Anderson [7] found expected species concentrations present at the stagnation point of a reentry spacecraft at various altitudes; one of our goals was to replicate the same trends using our novel chemical equilibrium calculator. Results are shown in Fig. 17. Although the simulation plot is not validated exactly, it is noteworthy that the general regions of each mode generally agree with Anderson's plot. The same issues present in the equilibrium composition by pressure in Figs. 15b - 16b are likely the reasons why this simulation did not converge exactly for all cases tested. Even so, the model did

produce reasonably close results and was a satisfactory accomplishment for the fundamental study being undertaken here.

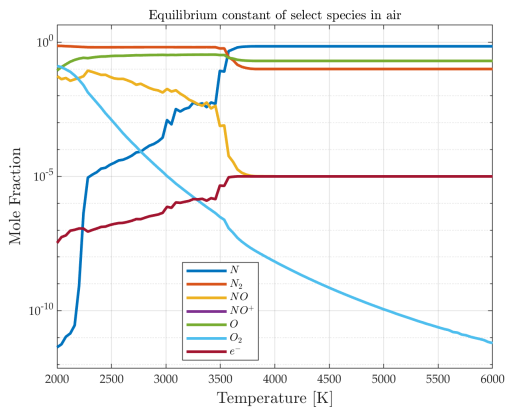


(a) Composition of equilibrium air vs temperature at 1 atm. Courtesy of [7]

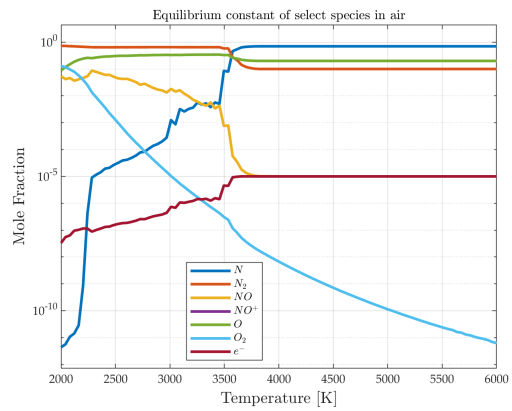


(b) Our air composition equilibrium model at 1 atm.

Fig. 15 Literature vs simulation results for atmospheric gas species mole fractions

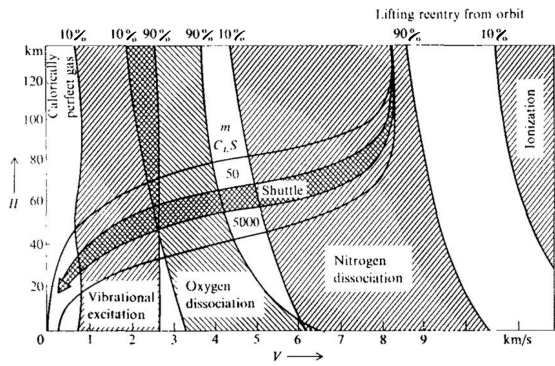


(a) Composition of equilibrium air at 0.1 atm.

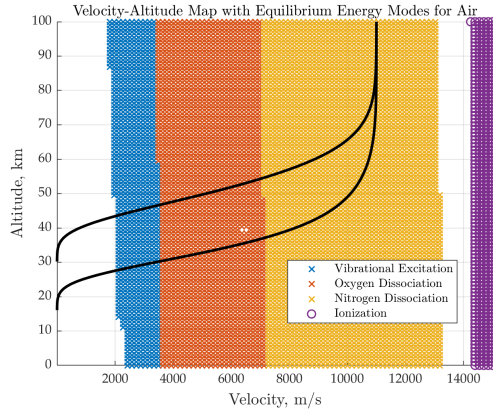


(b) Composition of equilibrium air at 0.01 atm.

Fig. 16 Equilibrium constant for select atmospheric gases in Earth's atmosphere at 0.1 and 0.01 atm pressures.



(a) Literature results from [7].



(b) Simulation results

Fig. 17 Literature plot and simulation results showing vibrational excitation, oxygen and nitrogen dissociation, and ionization of atmospheric gas species during hypersonic reentry.

C. Stagnation Pressure and Temperature Results

Results obtained from an earlier study ([9]) are presented here, since this section is concerned with obtaining the stagnation pressure and temperature at the stagnation point of a reentry object. The plot in Fig. 18 shows expected trends for both stagnation temperature and pressure for a reentry object. Importantly, note that the very high stagnation temperatures are taken using the full kinetic energy model of a reentry craft; that is, anything above vibrational excitation (namely dissociation and ionization) are not considered in this plot. Thus, the stagnation temperature actually seen by the wall of the reentry object would be substantially lower.

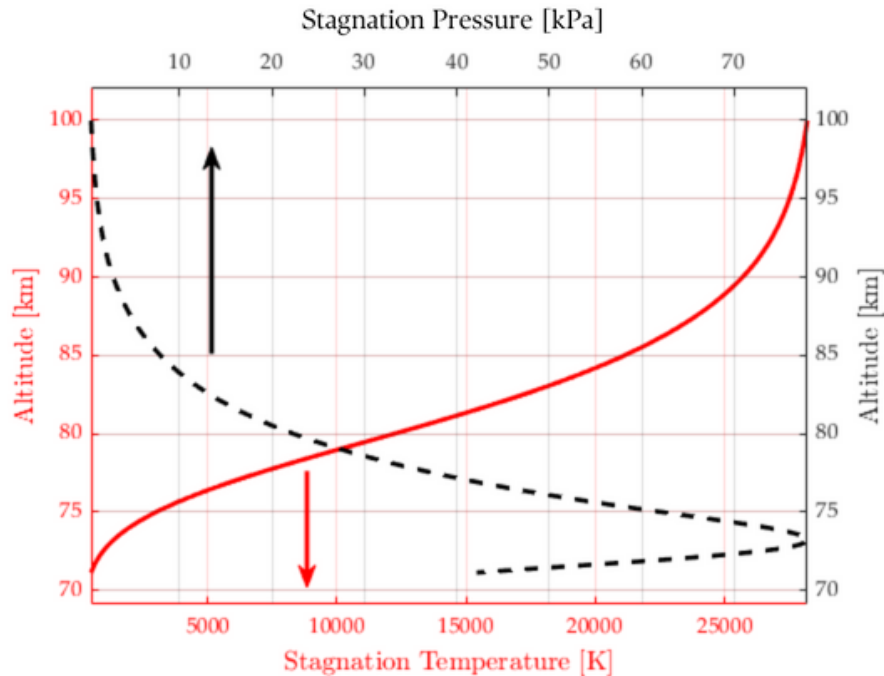


Fig. 18 Stagnation temperature and pressure modelled at the forward-most facing part of the deorbiting spacecraft. Maximum heating and consequent burnup likely happens around 75 km altitude, and around 70 km the vehicle (if any remains) goes subsonic and normal shock assumptions fail. Changes below this altitude are negligible and the flow is treated as isentropic. Arrows indicate associated plot axes.

D. Computational Fluid Dynamics of a Sphere Results

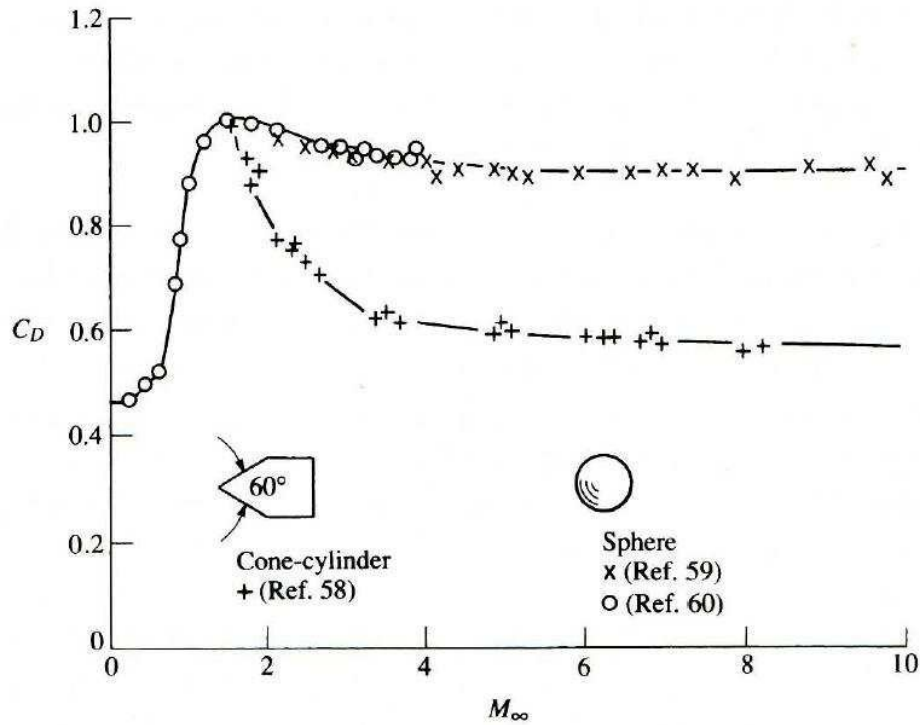
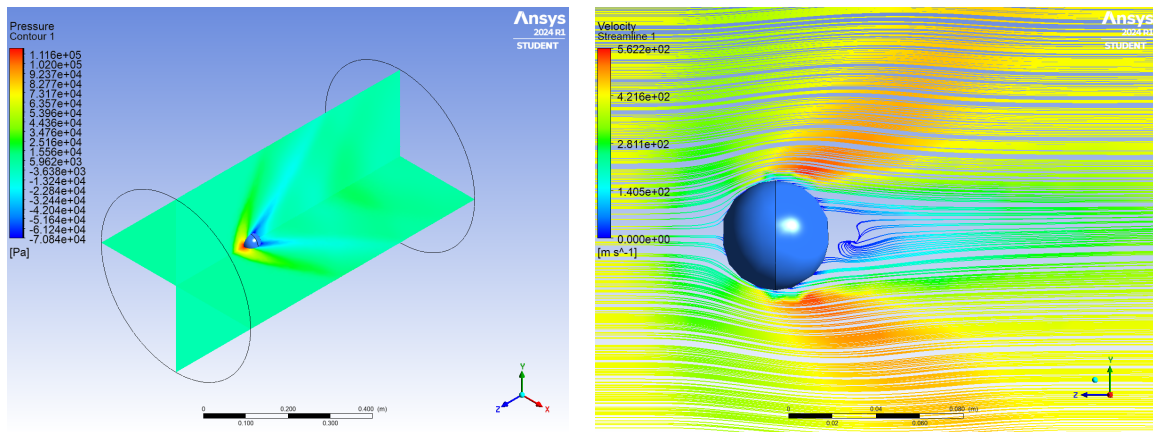


Fig. 19 Literature values for simulation validation. Taken from [10].

1. Supersonic Steady Flow



(a) Pressure distribution at Mach 1.2

(b) Velocity and streamlines at Mach 1.2

Fig. 20 Supersonic steady flow at Mach 1.2.

The pressure and velocity contour results in all cases exhibited expected trends. The flow velocity stagnated at the front of the object at the normal shock point, where the pressures were also highest.

Most notably, the plot shown in Fig. 26 agrees remarkably well with literature values (see Fig. 19) for all Mach numbers tested. The simulations were thus reasonably validated against literature results.

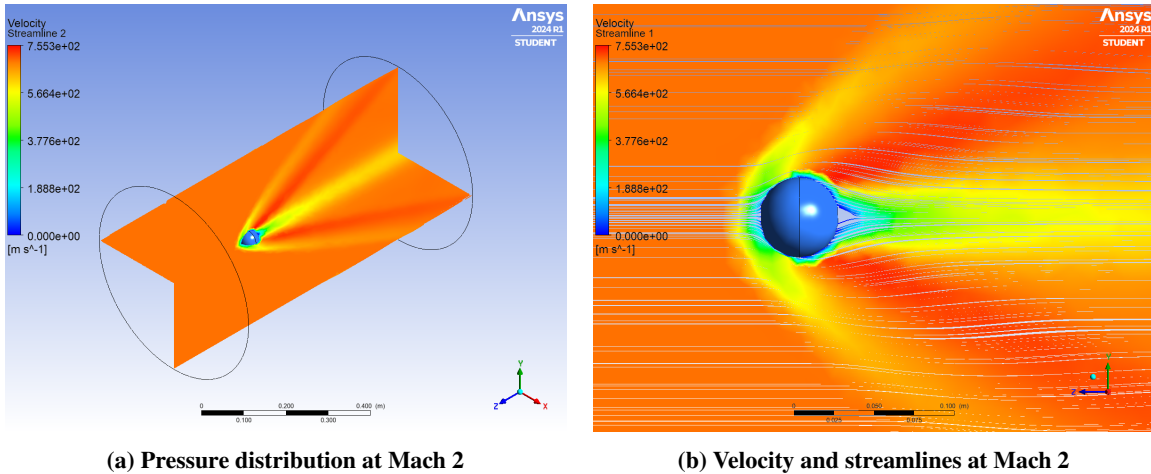


Fig. 21 Supersonic steady flow at Mach 2.

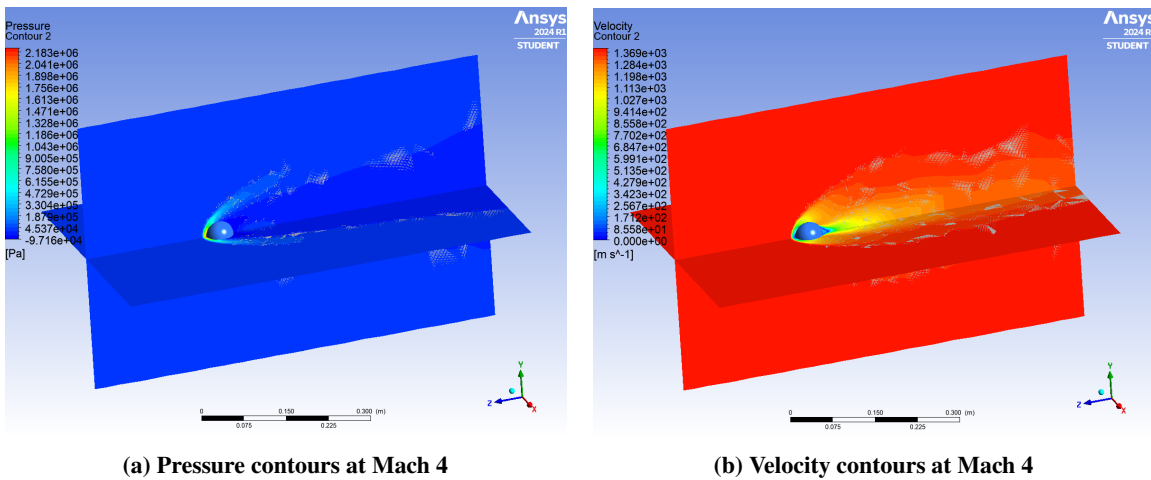


Fig. 22 Supersonic steady flow at Mach 4.

2. Supersonic Unsteady Flow

The pressure and velocity contours for the supersonic transient flow cases were examined and exhibited behavior as expected. Although an animation is not visible in this paper, the still shots display expected flow characteristics for a supersonic flow. Due to issues in the solver for high Mach cases, the supersonic case was conservatively taken to be Mach 1.1.

3. Subsonic Steady Flow

For all cases, the simulations produced expected results. The pressure, velocity, and streamline cases all exhibited flow behavior as expected from an incompressible, isentropic standpoint. Notice especially how the C_D vs Mach plot in Fig. 35, compares with the literature plot in Fig. 19 for low Mach numbers. Although the values obtained in the simulations are not exact, the general trend is in agreement with literature.

4. Subsonic Steady Flow

Both C_D vs Mach plots from the steady supersonic and subsonic simulations agreed reasonably well with literature ([10]) and shown in Fig. 19. If more transient cases were tested, a plot could be developed that might be interesting. In general, the drag coefficients followed the expected trend: for subsonic, C_D is expected to increase, then reach a peak just over Mach 1. The drag force equation yields some intuition:

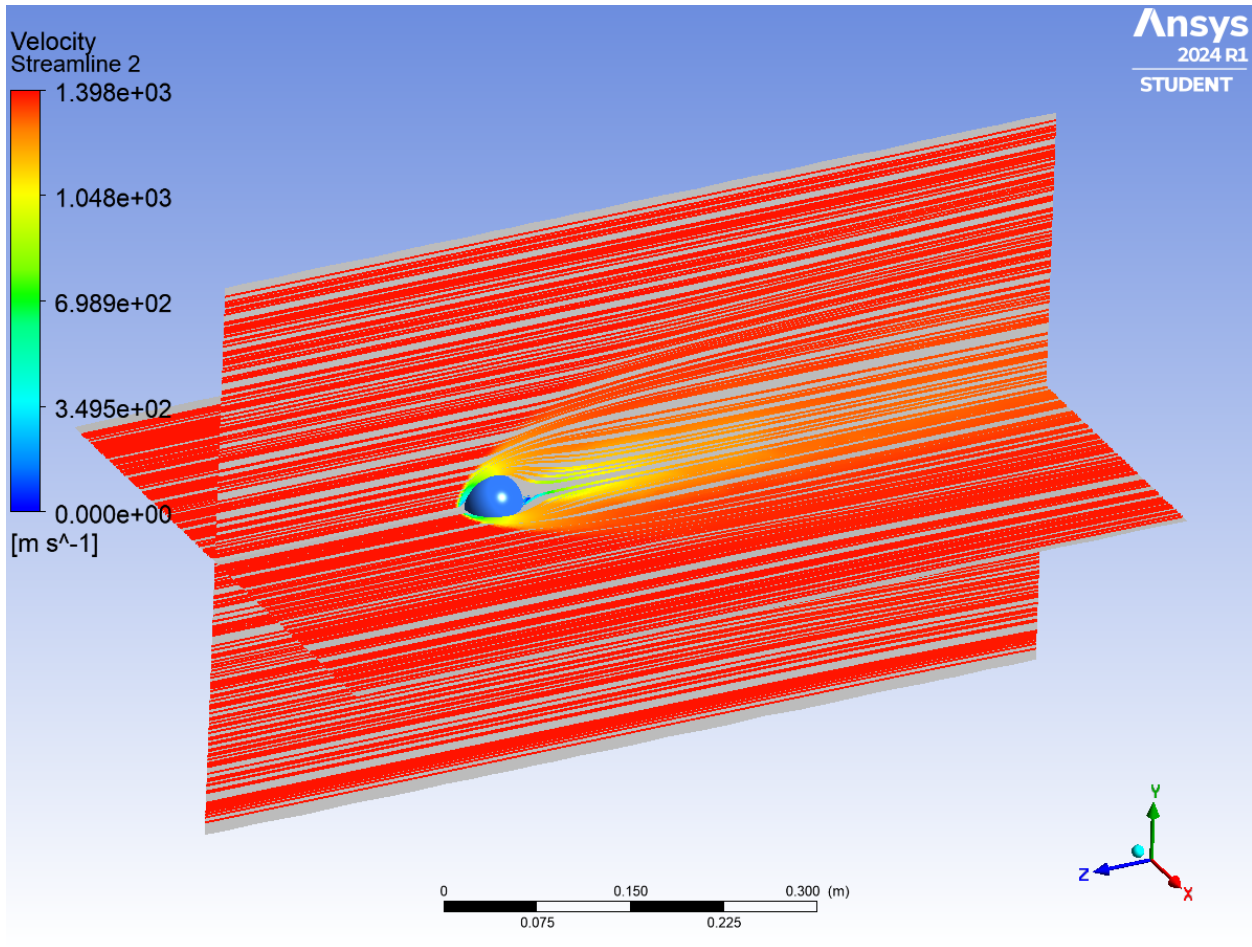
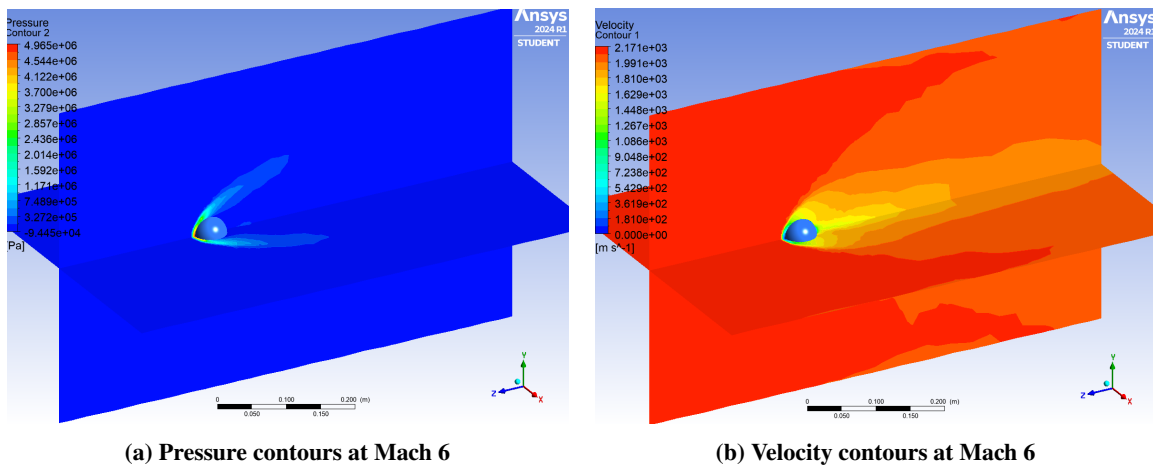


Fig. 23 Velocity streamlines at Mach 4



(a) Pressure contours at Mach 6

(b) Velocity contours at Mach 6

Fig. 24 Supersonic steady flow at Mach 6

$$F_D = \frac{1}{2} \rho v^2 C_D A$$

Notice that drag force and drag coefficient are highly dependent upon the reference area for given freestream

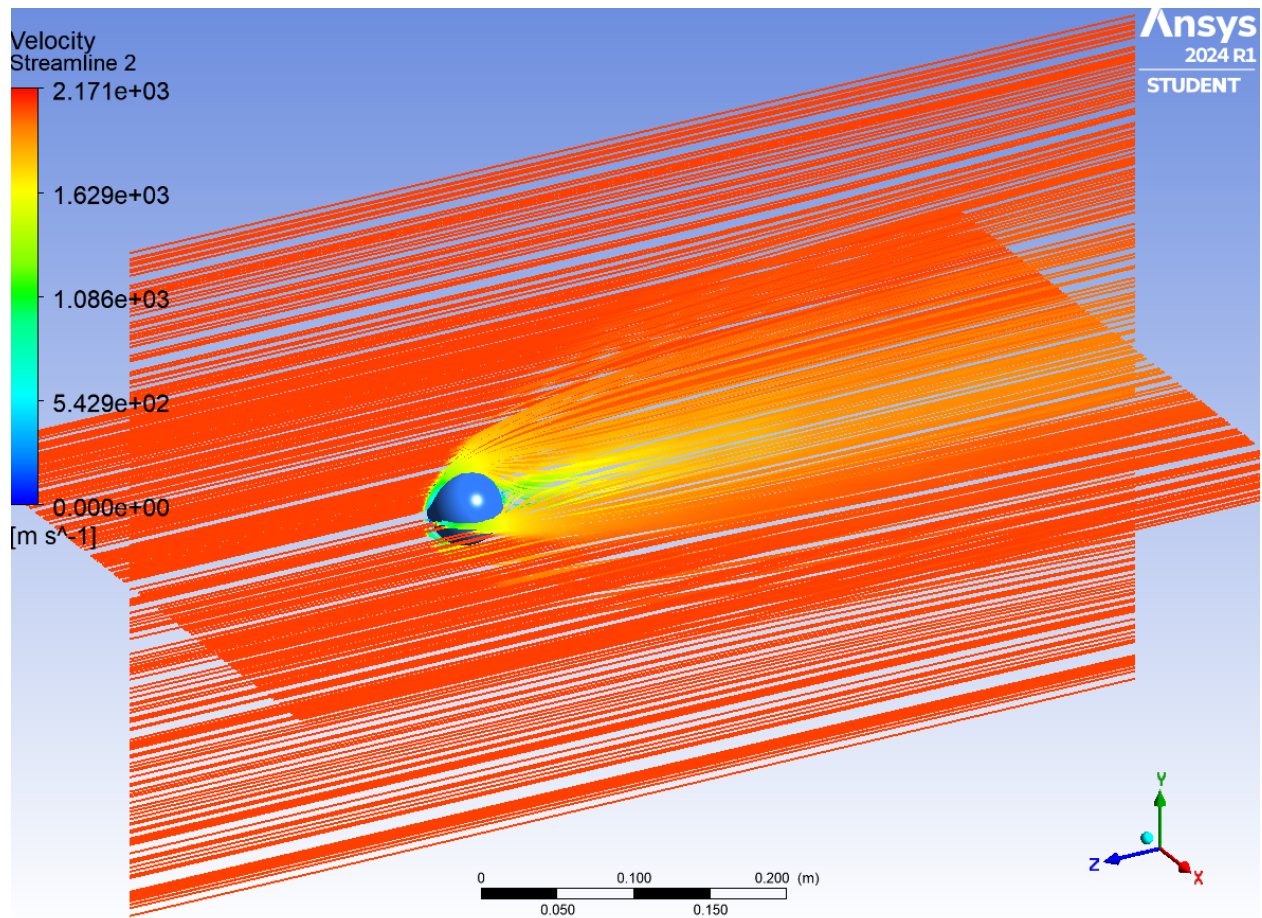


Fig. 25 Velocity streamlines at Mach 6

conditions. Thus, more tests at the given reference area would be recommended to increase confidence in our results. Note that all these tests used a sphere with radius of 25 mm.

A plot of drag coefficient vs. Mach for all simulations are shown in Fig. 38.

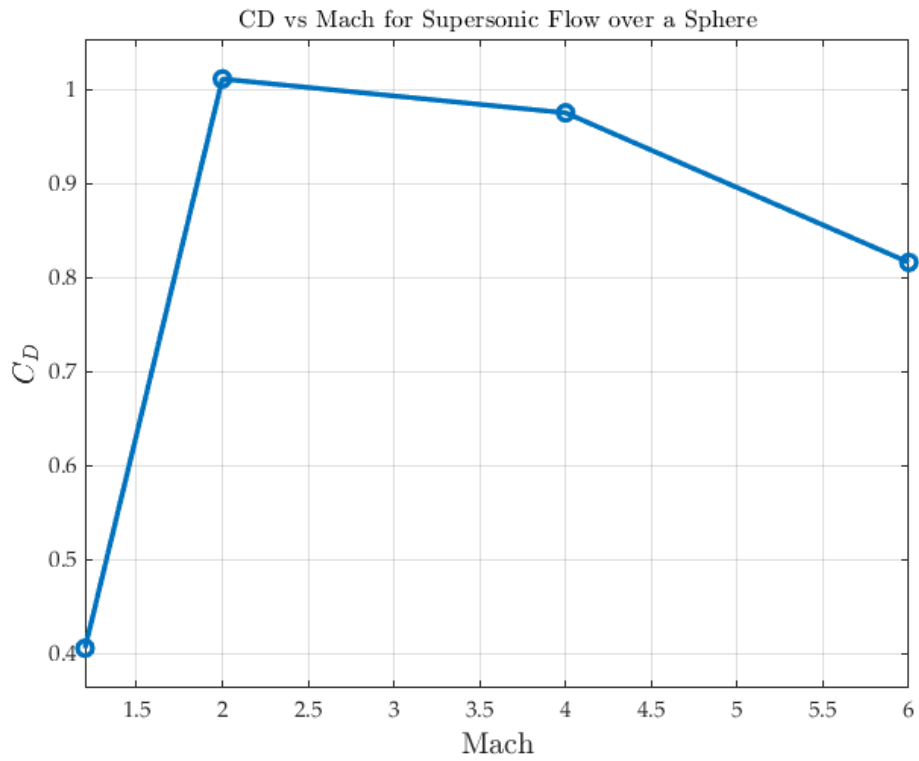


Fig. 26 Simulation results for supersonic steady flow cases studied.

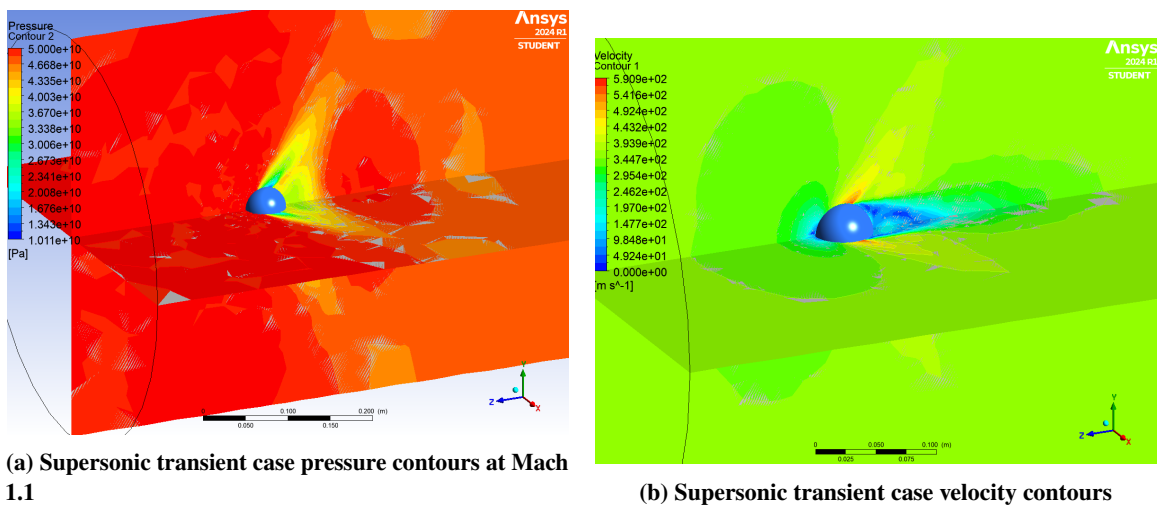


Fig. 27 Transient flow pressure and velocity contours for supersonic case ($M = 1.1$).

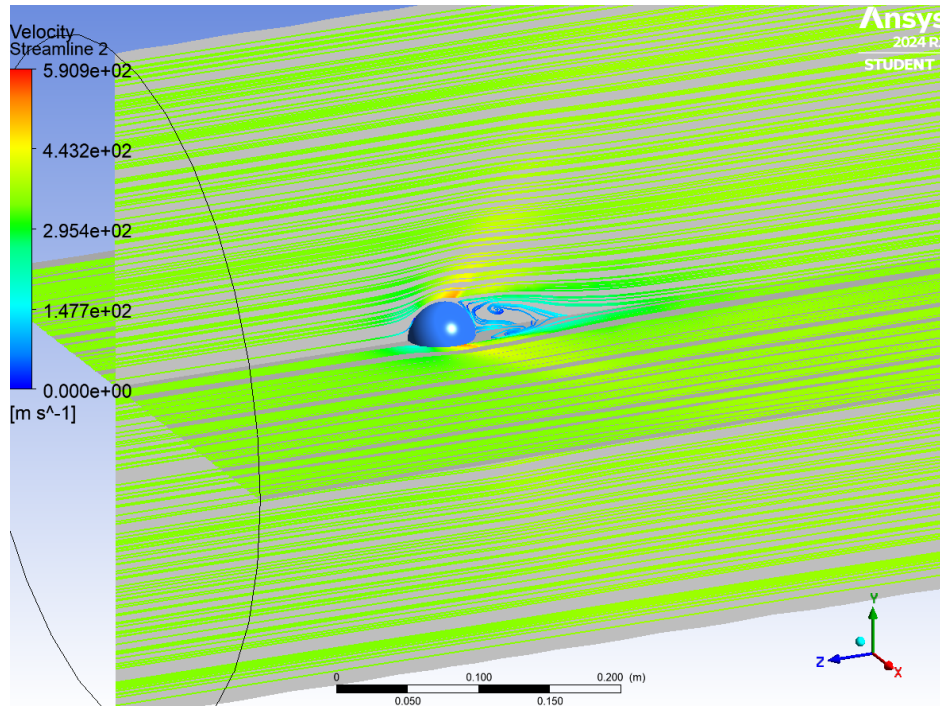
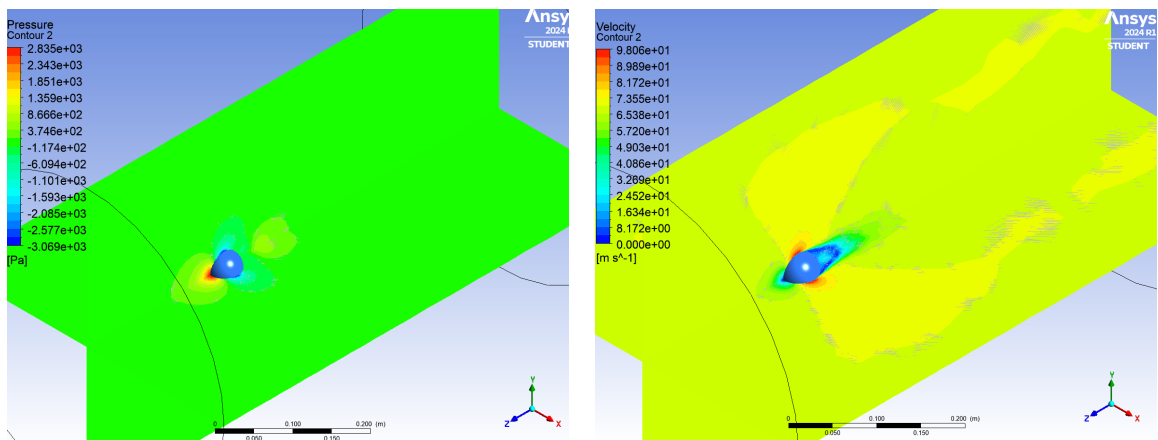


Fig. 28 Flow streamlines for supersonic transient flow case



(a) Pressure contours at Mach 0.2

(b) Velocity contours at Mach 0.2

Fig. 29 Steady flow pressure and velocity contours for $M = 0.2$.

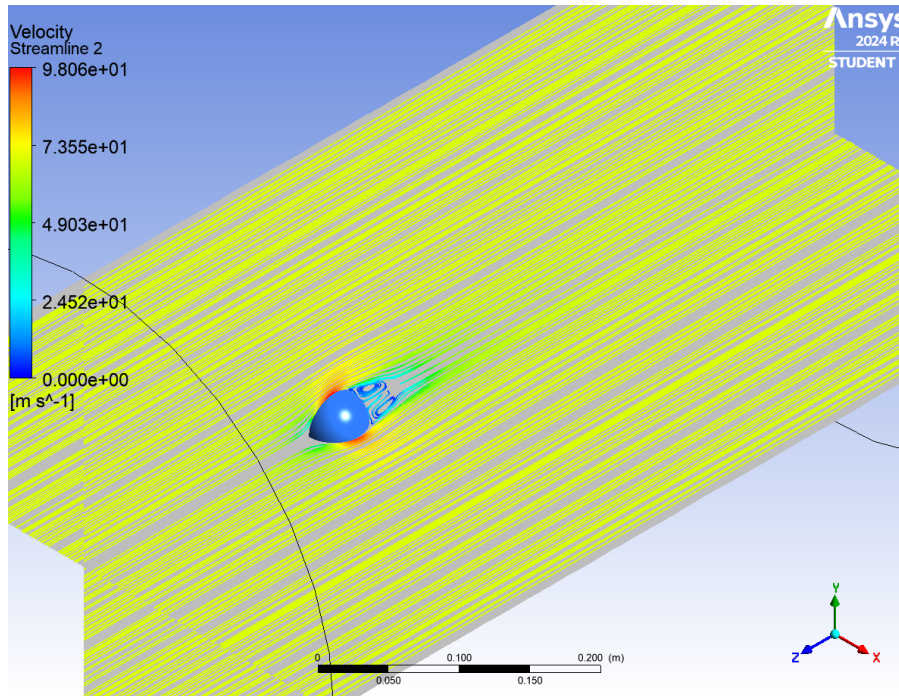
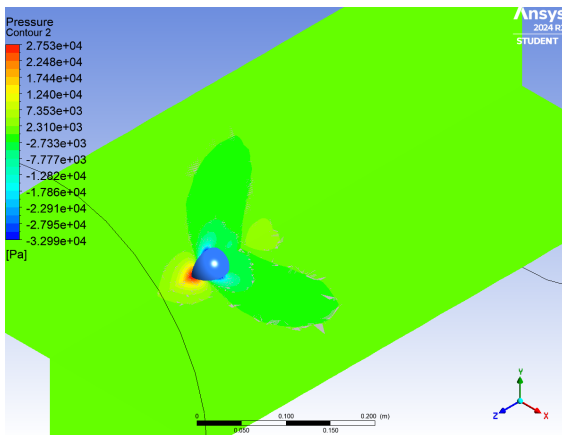
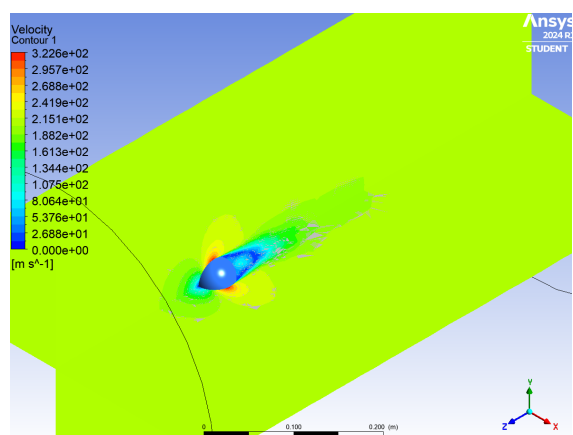


Fig. 30 Steady flow streamlines at Mach = 0.2.



(a) Pressure contours at Mach 0.6



(b) Velocity contours at Mach 0.6

Fig. 31 Steady flow pressure and velocity contours for M = 0.6.

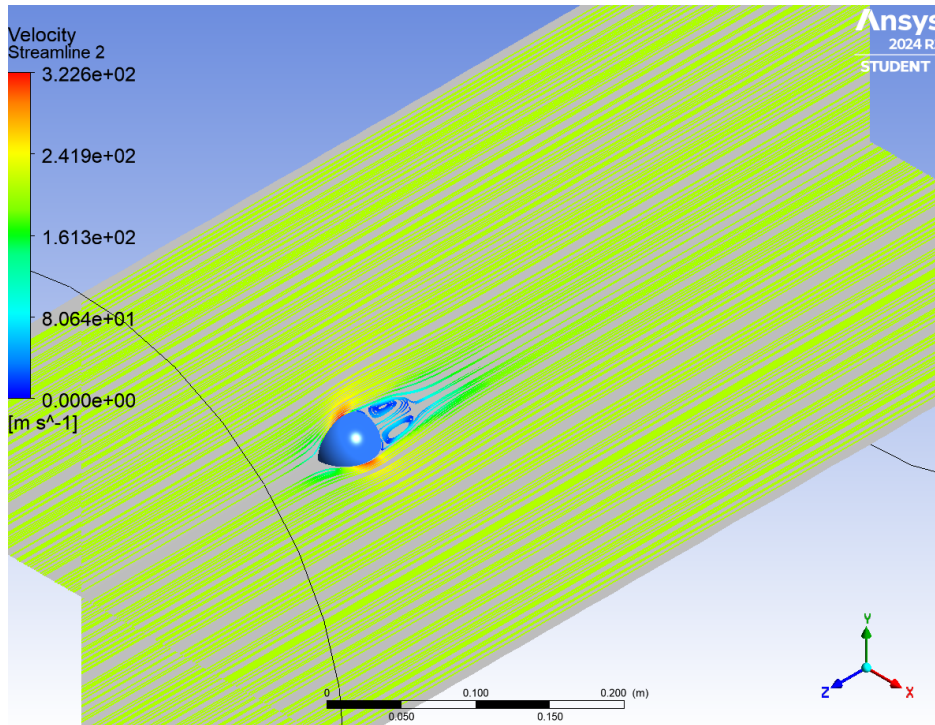
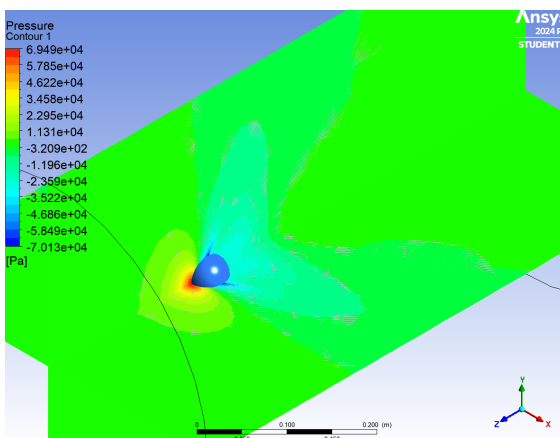
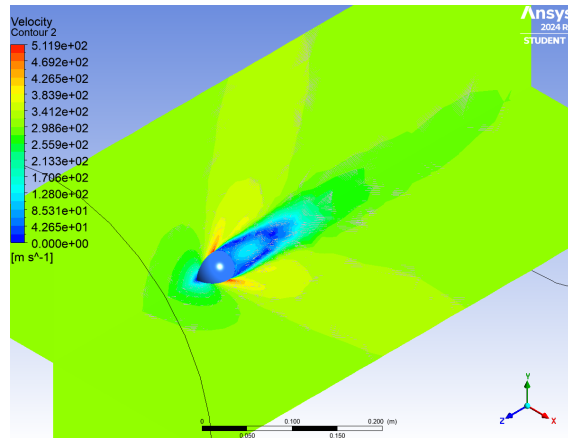


Fig. 32 Steady flow streamlines at Mach = 0.6.



(a) Pressure contours at Mach 0.9



(b) Velocity contours at Mach 0.9

Fig. 33 Steady flow pressure and velocity contours for M = 0.9.

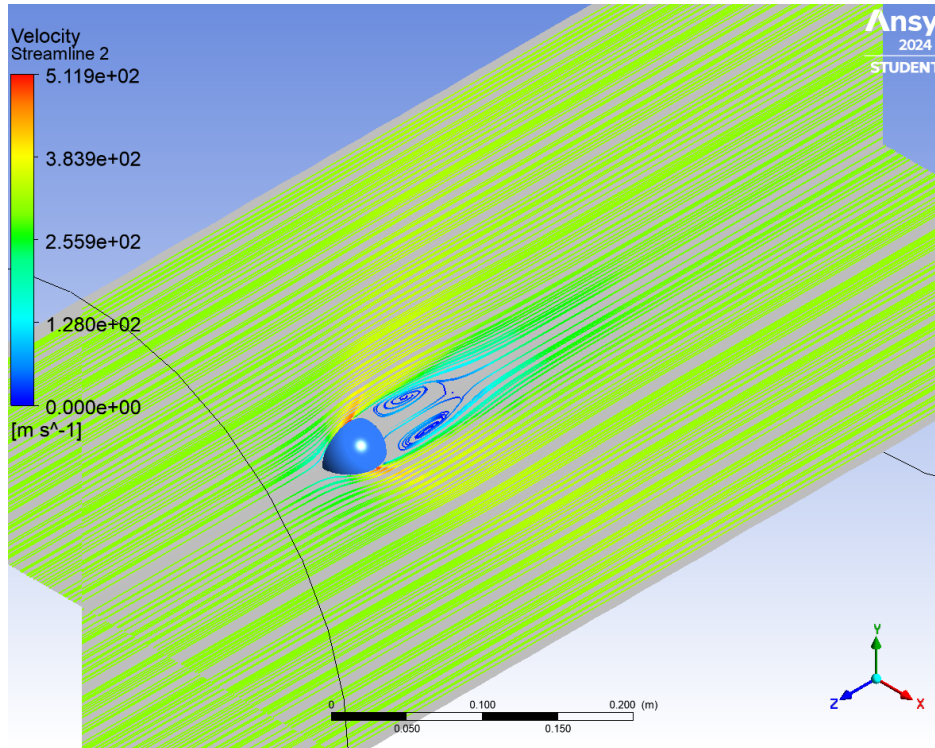


Fig. 34 Steady flow streamlines at Mach = 0.9.

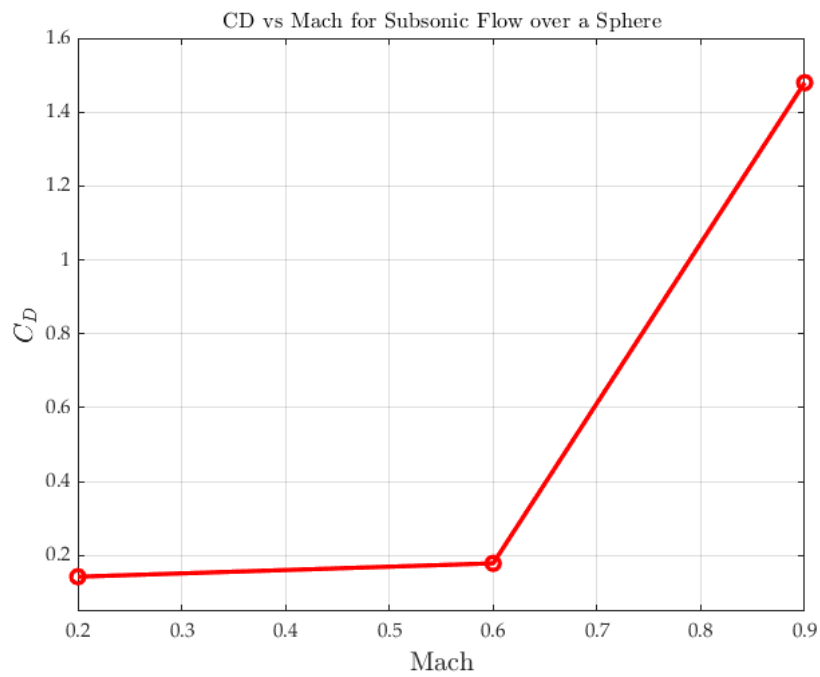
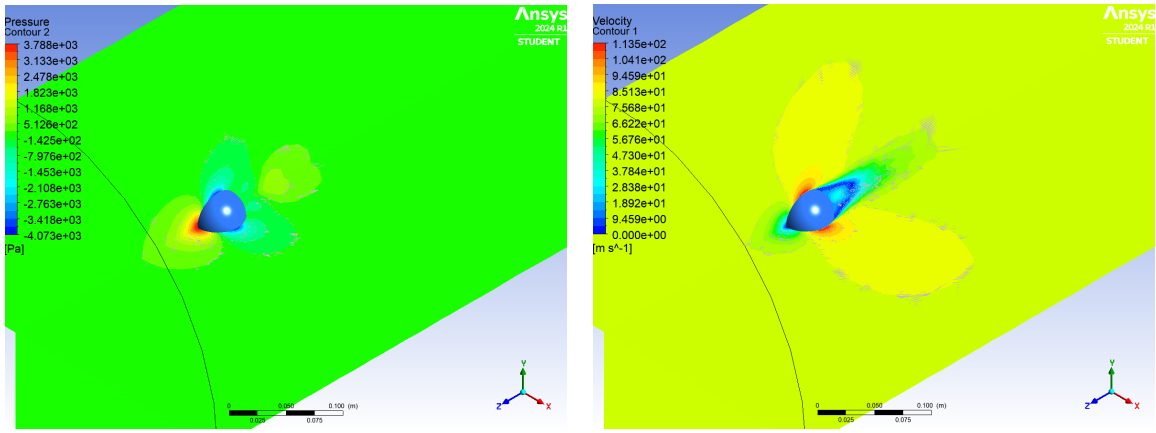


Fig. 35 Subsonic steady flow. Notice the general correlation with literature values for low Mach numbers in Fig. 19.



(a) Subsonic transient case pressure contours

(b) Subsonic transient case velocity contours

Fig. 36 Transient flow pressure and velocity contours for subsonic case ($M = 0.2$).

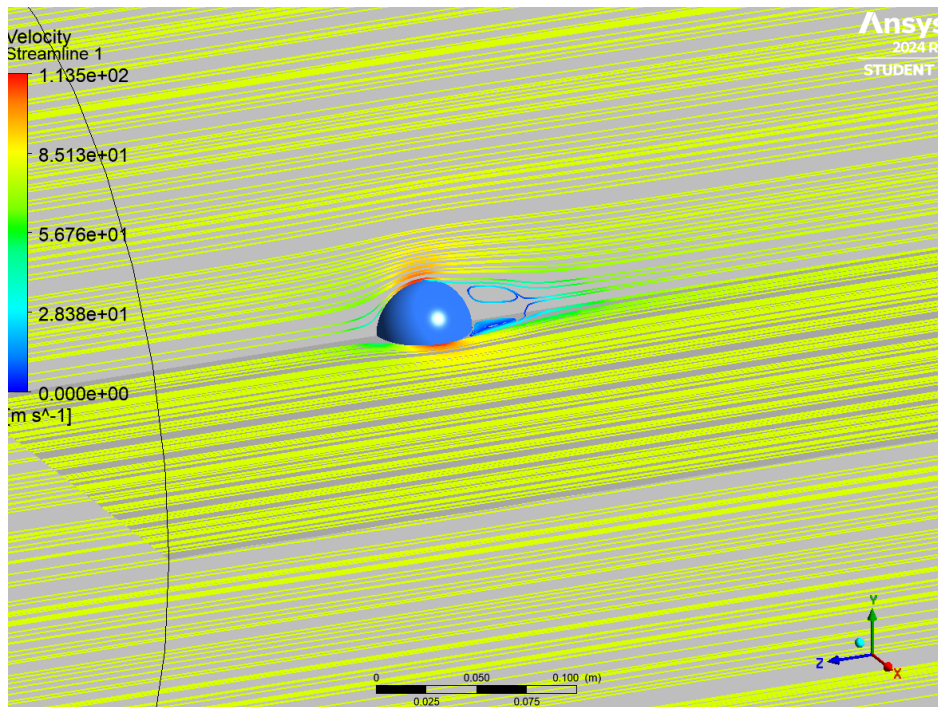


Fig. 37 Streamlines for subsonic transient flow case

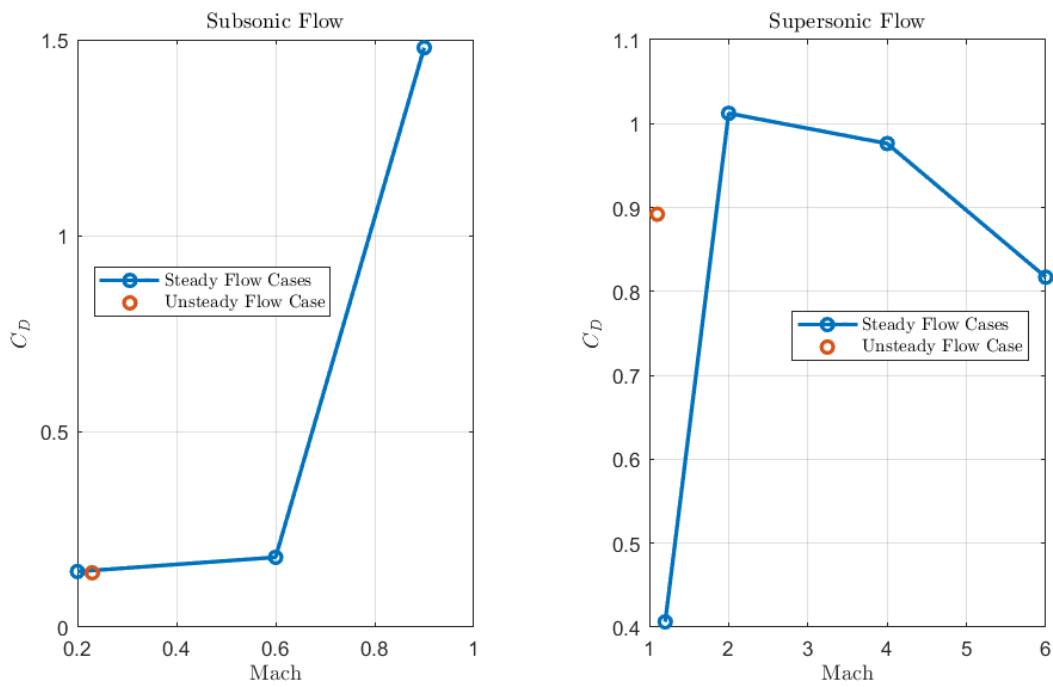


Fig. 38 C_D vs Mach for all simulation cases

V. Conclusion

Reentry flight studies are vital for the design and analysis of human and sample return space missions, to name a few recent examples. The reentry picture is more than an entry, descent, and landing engineering scheme. The full reentry profile and aerothermal chemistry interactions with the local atmosphere must be taken into consideration with reentry heating and hypersonic boundary layer theory taking a front seat. This review paper briefly summarized the fundamentals of the following subjects:

- Reentry flight regimes and orbital trajectories
- Atmospheric composition and equilibrium state
- Reentry flight mechanics, range, and ballistic profile
- Aerothermal chemistry, thermally-perfect gas case, and parameters affecting c_v
- Hypersonic aerodynamics, boundary layer theory, reentry heating
- Computation fluid dynamics modelling of supersonic and subsonic flow regimes

A lunar free-return trajectory similar to that of the Apollo program was simulated from a 320 km circular parking orbit to a lunar flyby at a perilune of 1021.7 km altitude. The total Δv for the single impulsive burn at TLI was 3.0526 km/s. The total mission time elapsed was 166.5 hours, and the final atmospheric reentry (at Earth) occurred at 100 km altitude with a velocity of about 11 km/s and a reentry flight path angle, γ , of -23.7° .

The flight reentry corridor, plotted as altitude vs. velocity, was characterized for an array of ballistic coefficients to simulate tumbling or spacecraft breakup. Simulations were run for varying flight path angle for a “flat earth” geometry. However, the results agreed reasonably well with similar plots in literature. It was found that a deployable heat shield reduced the impact velocity proportionally to (not surprisingly) a larger drag coefficient, for a range of 54 - 49.5 m/s corresponding to drag coefficient increases of 10, 50, and 100 percent, respectively. However, it is clear that more than just a heat shield would be needed to slow down an orbital crewed mission with a nominal splashdown velocity of < 11 m/s.

In the aerothermal chemistry section, a chemical equilibrium calculator was developed (see Appendix A) that produced results consistent with JANAF and NASA tables for most gases studied. The outputs from the validated program were used to calculate various energy modes and, thus, equilibrium constants and eventually mole fractions of gas species present in earth's upper atmosphere. Although the numerical solver did not produce results as smooth as we would have liked, this work provides a useful baseline approach for the numerical scheme. It is recommended to utilize a more robust solver that is less sensitive to initial guesses, since some of the guesses may be unknown to the precision required by the solver.

Stagnation pressure and temperature for a sphere at reentry velocity and altitude were plotted from ([9]). It is understood that the high reported values of stagnation temperature are from an initial standpoint, that is, that all the kinetic energy of the orbital reentry object is not going to the walls of the object, but rather is being used to heat the flow around the object, as discussed in the introduction.

Computational results agreed reasonably with literature values for drag coefficient of a sphere in super- and subsonic regimes. The same trend was observed for both the supersonic and subsonic flow simulations, although the magnitude of C_D differed slightly in each case. More simulations across multiple flow regimes is recommended for further analysis and validation.

References

- [1] Hankey, W. L., *Re-entry aerodynamics*, Aiaa, 1988.
- [2] Citruzz, W., *Perifocal Coordinates*, 2023. URL https://en.wikipedia.org/wiki/Perifocal_coordinate_system#/media/File:Perifocal_coordinates.svg.
- [3] Kim, E., Han, S., and Sayegh, A., “Sensitivity of the Gravity Model and Orbital Frame for On-board Real-Time Orbit Determination: Operational Results of GPS-12 GPS Receiver,” *Remote Sensing*, Vol. 11, 2019, p. 1542. <https://doi.org/10.3390/rs11131542>.
- [4] Davies, C., and Arcadi, M., “Planetary mission entry vehicles quick reference guide. Version 3.0,” Tech. rep., 2006.
- [5] Curtis, H. D., *Orbital Mechanics for Engineering Students: Revised Reprint*, Butterworth-Heinemann, 2020.
- [6] Suresh, A., Ranjan, G., Harsha, S., Surya, K., Ranjan, A., Ajithkumar, N., Sabu, S., Teja, V., David, A. V., Sonkamble, S., et al., “Innovative Low Cost Mars Flyby Spacecraft for Safe Interplanetary Human Mission,” *Mars Society Convention, Marspapers*, 2016.

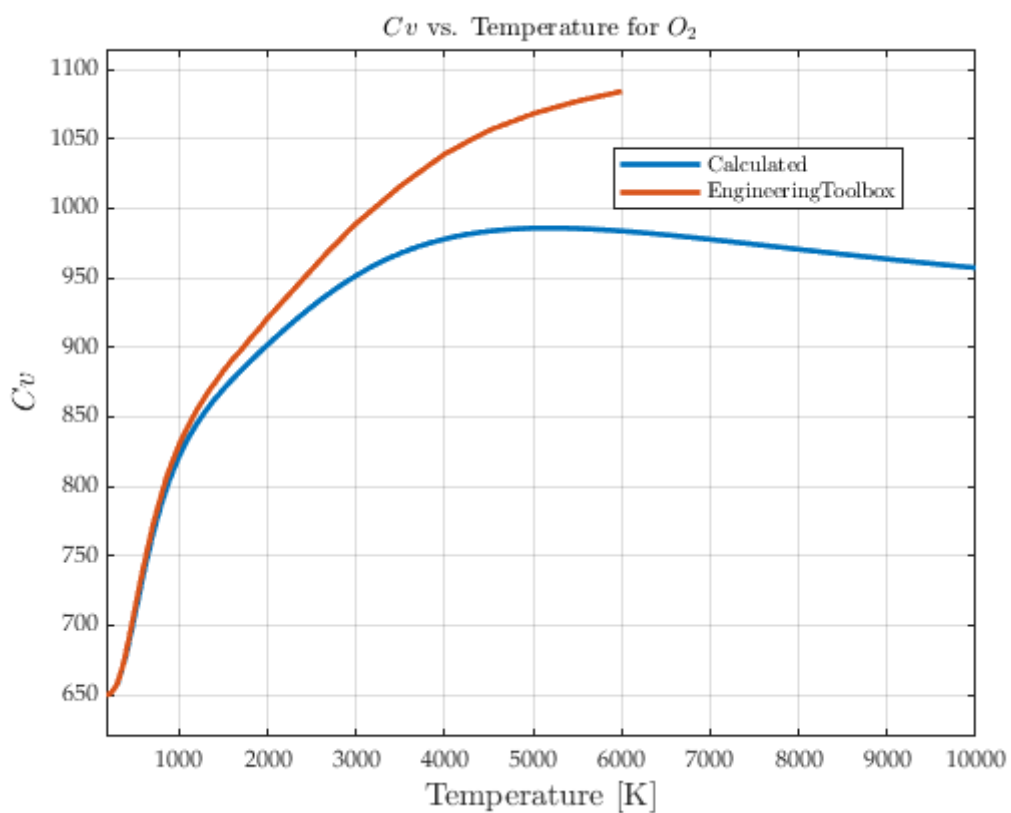
- [7] Anderson, J. D., *Hypersonic and high temperature gas dynamics*, Aiaa, 1989.
- [8] Stull, D. R., *JANAF Thermochemical Tables...*, Vol. 1, Clearinghouse, 1965.
- [9] Hiremath, N., Self, J., and Eller, N., "System Architecture for De-orbiting Spacecrafts as a Platform for Experimental Aerodynamics Studies," *IEEE Aerospace Conference. Big Sky, MT.*, 2024.
- [10] Dolya, S., "The movement of the iron balls in the near space," 2015.

Appendix A: Chemical Equilibrium Calculator Validation

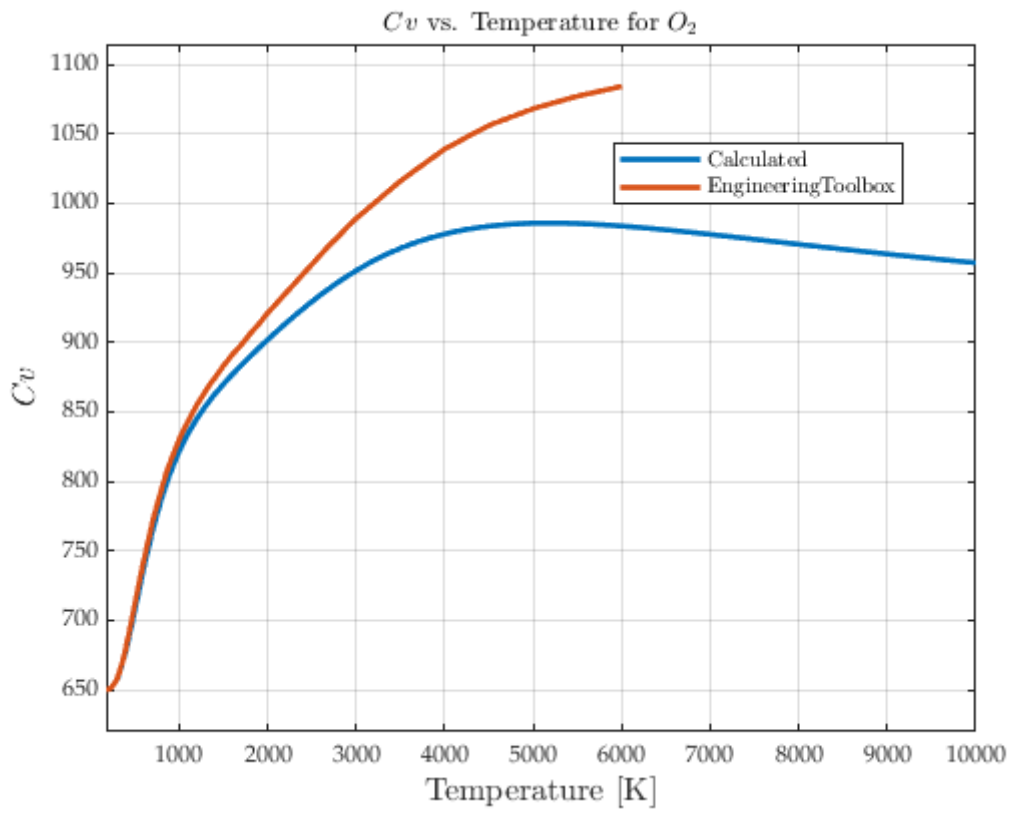
Table of Contents

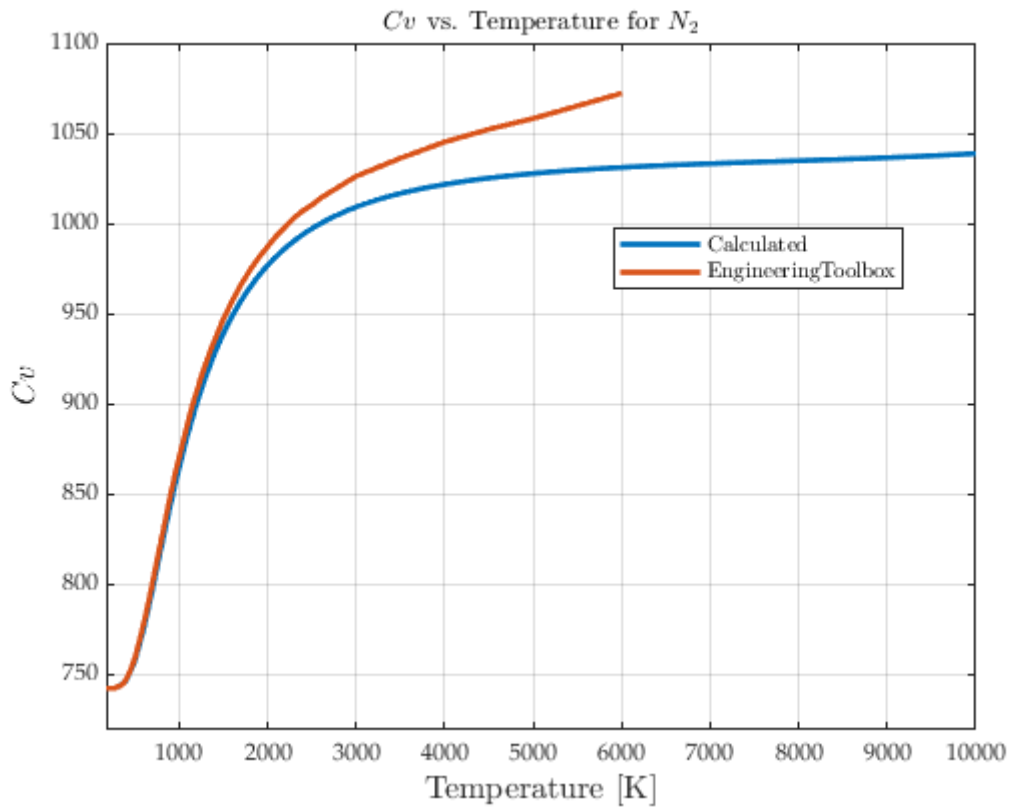
.....	1
O2	1
N2	2
N	4
O	6
NO	7
NO+	8
e-	10
CO2	11
Plot all	13
Plot Cv/R for all	14
Kp values (thermal equilibrium coefficients)	15

O2

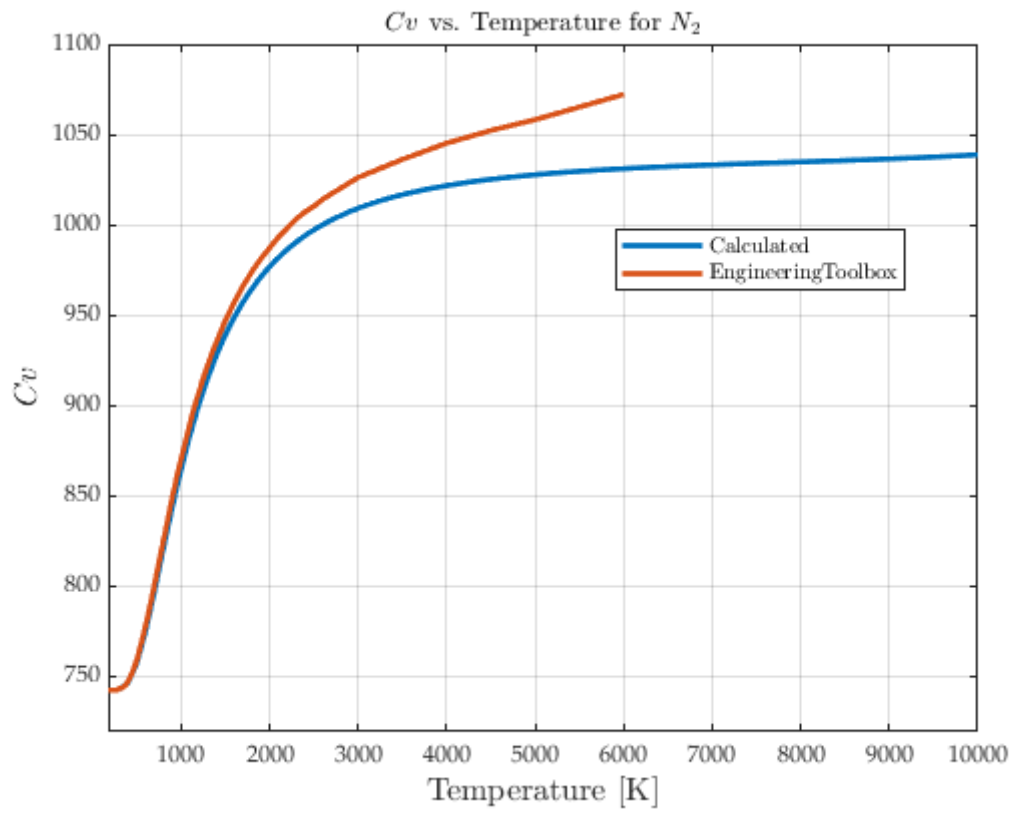


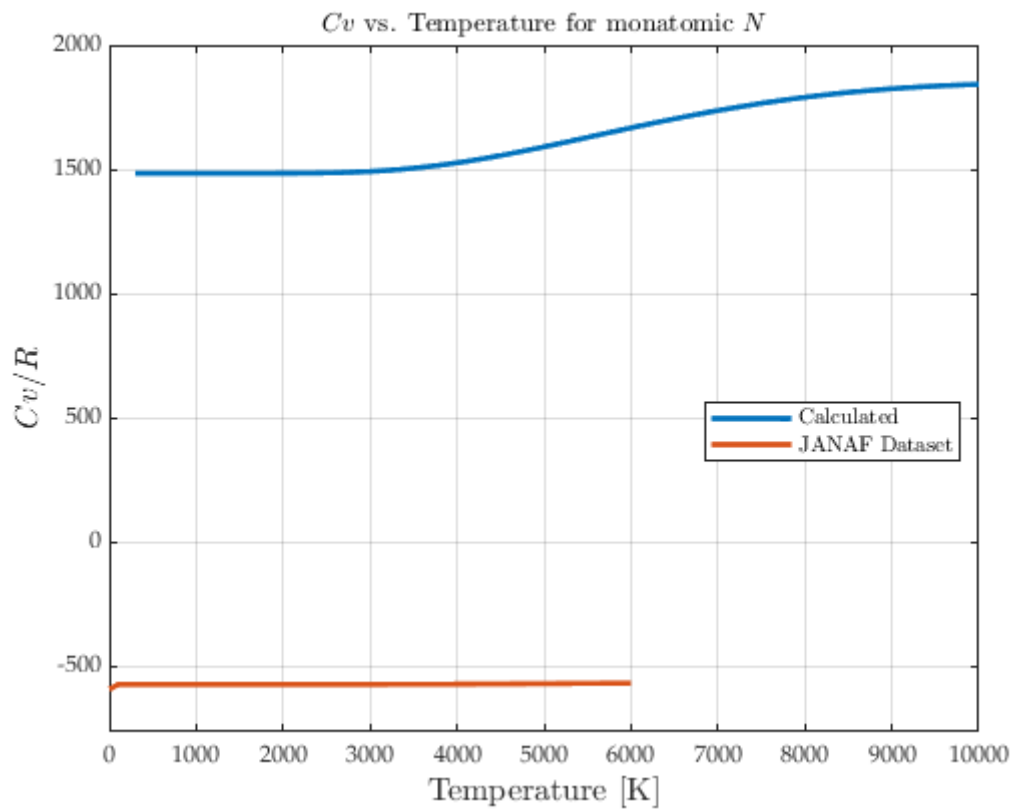
N2



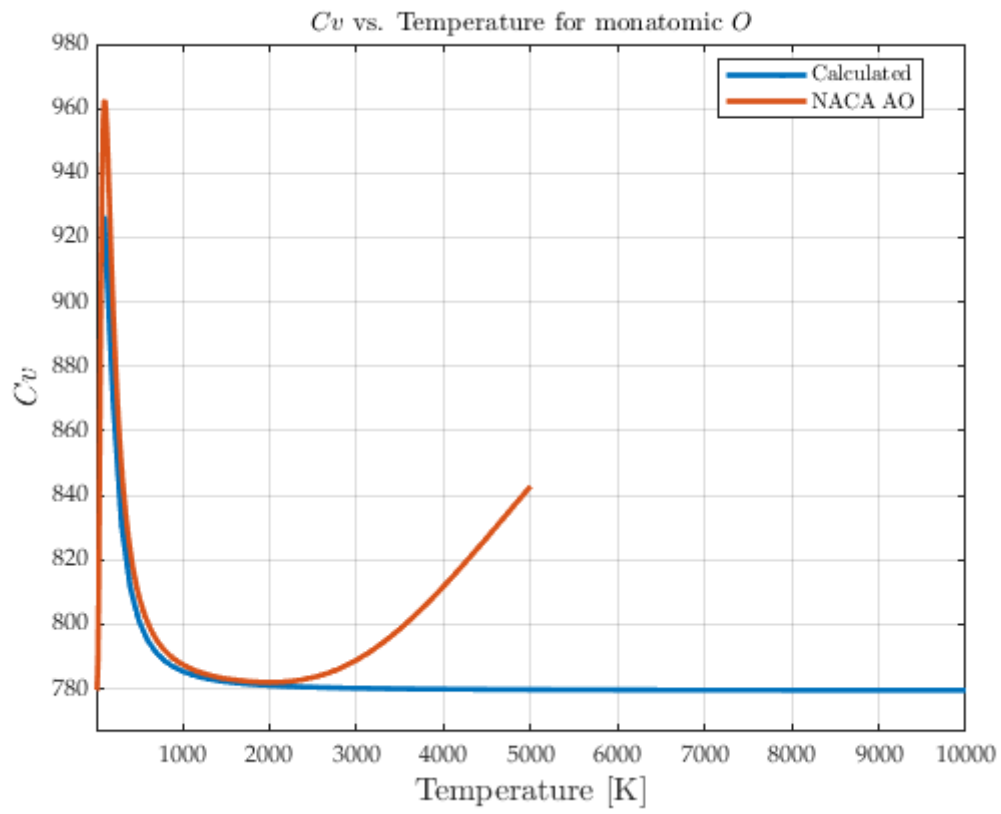


N

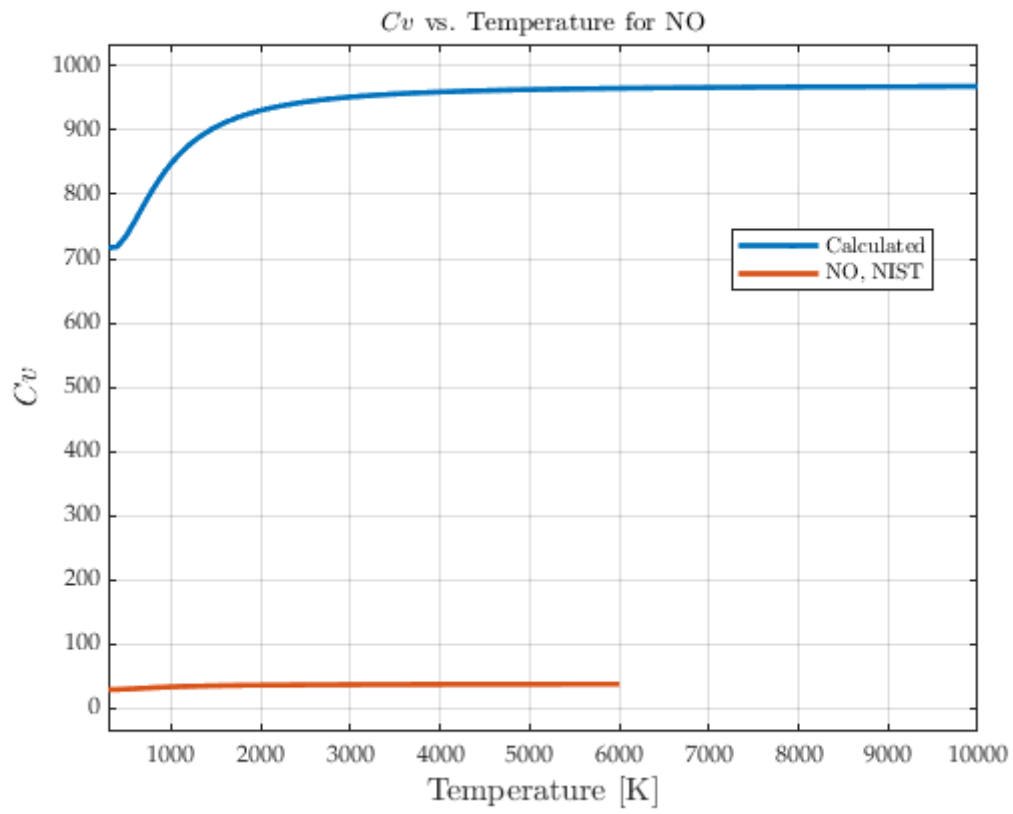




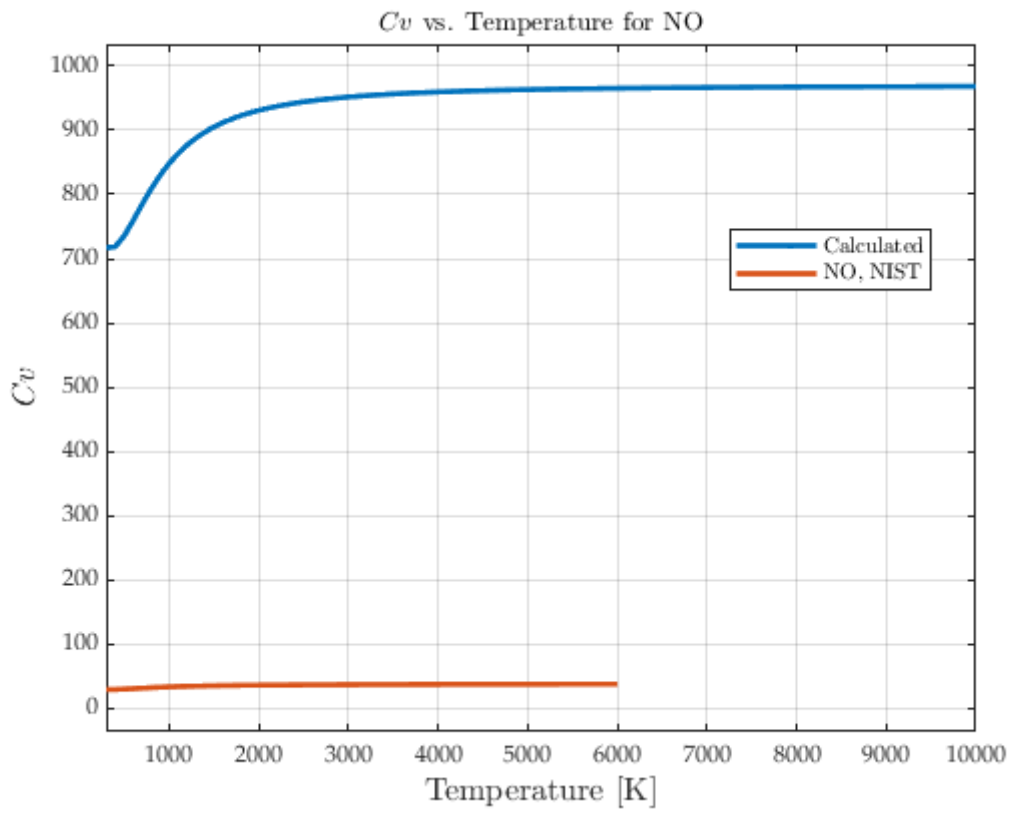
O

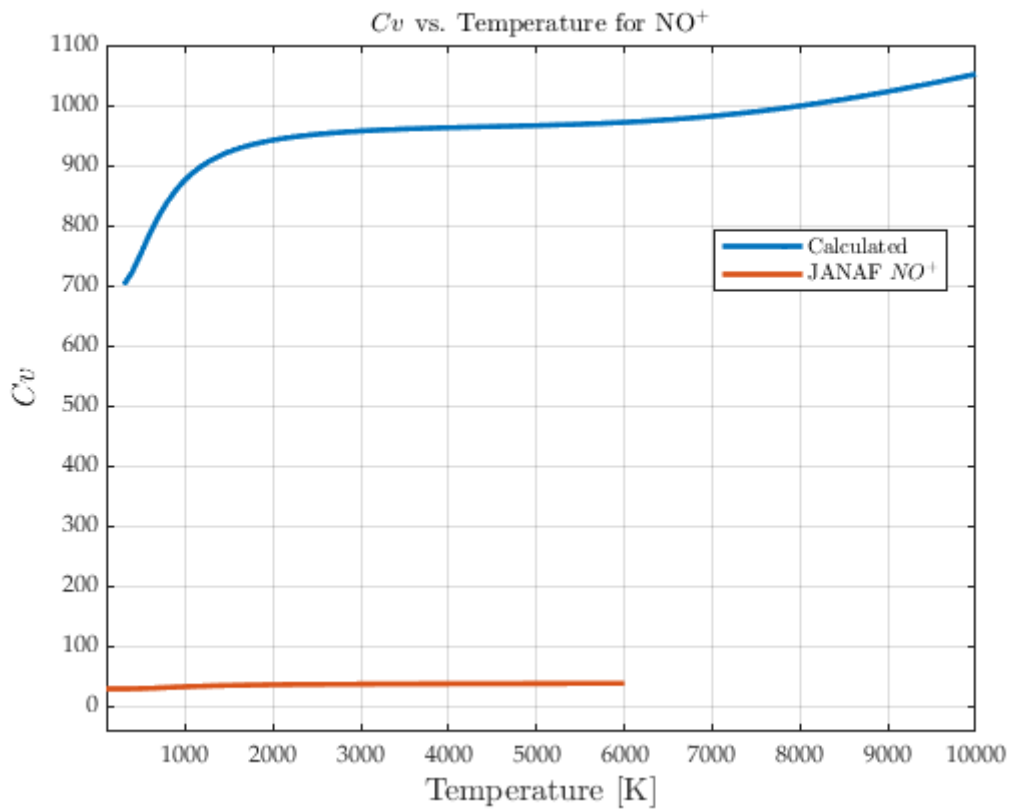


NO

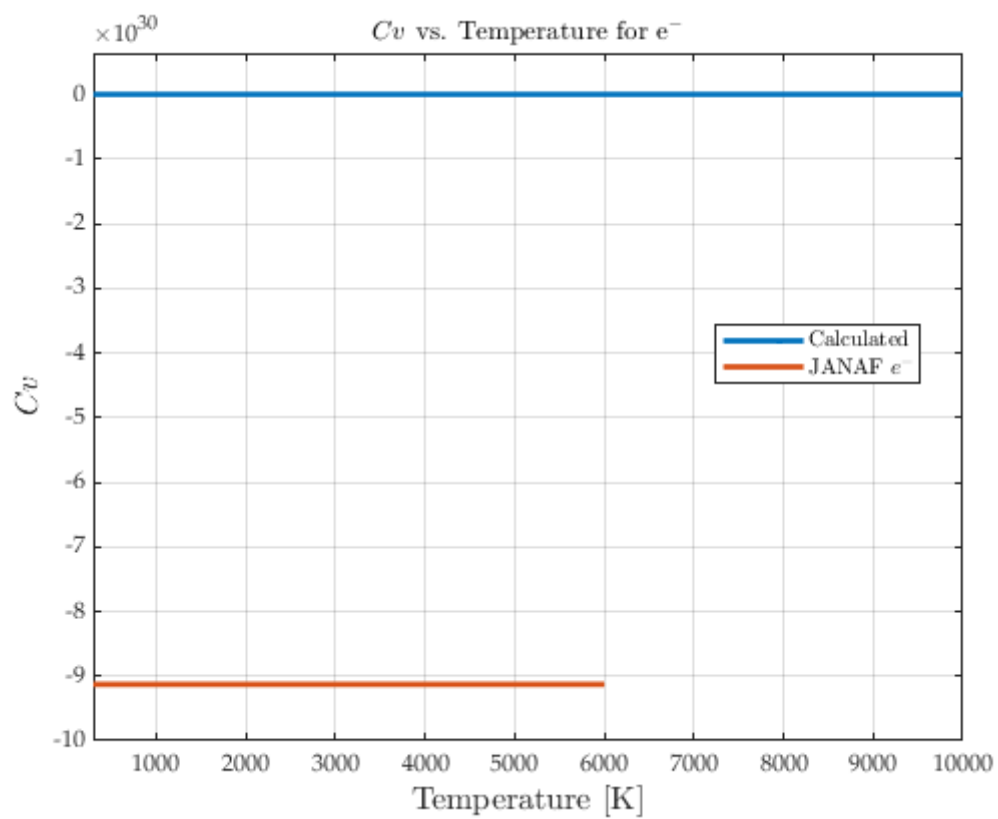


NO+

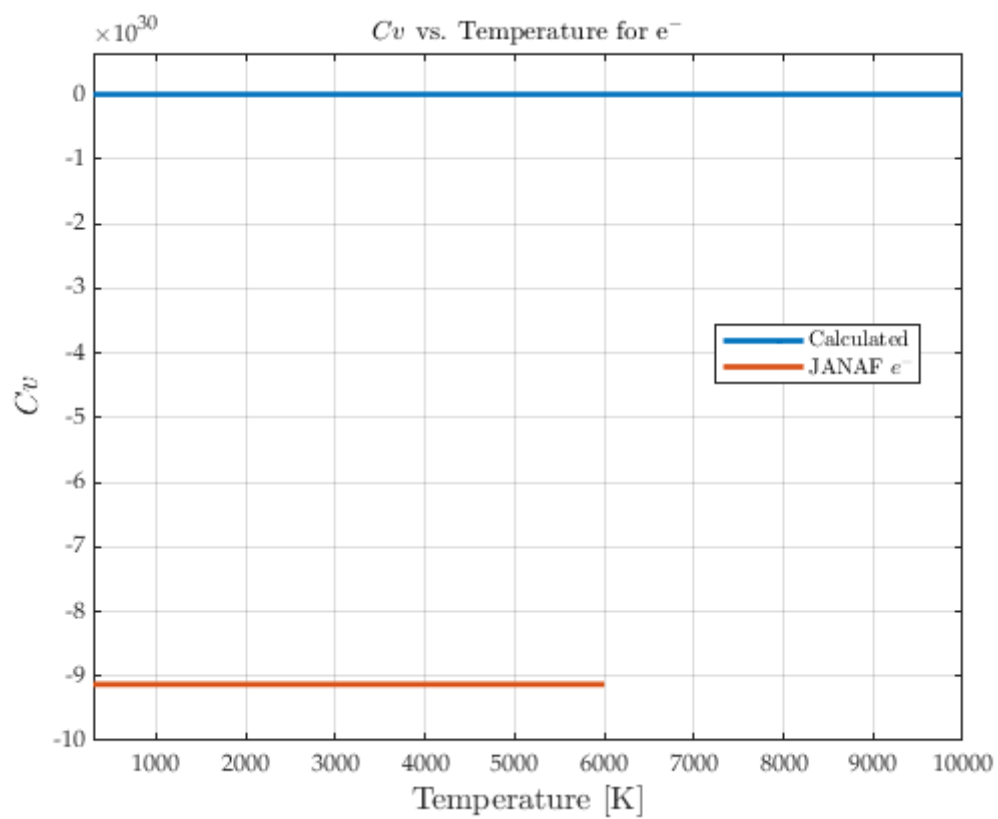


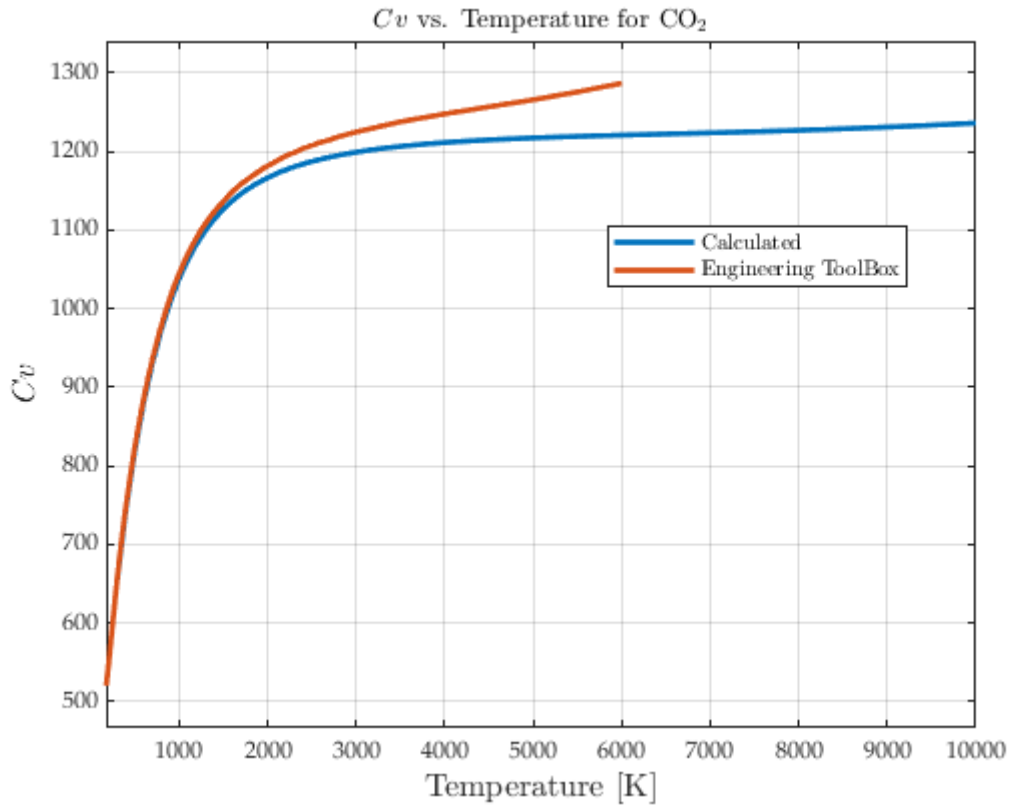


e-

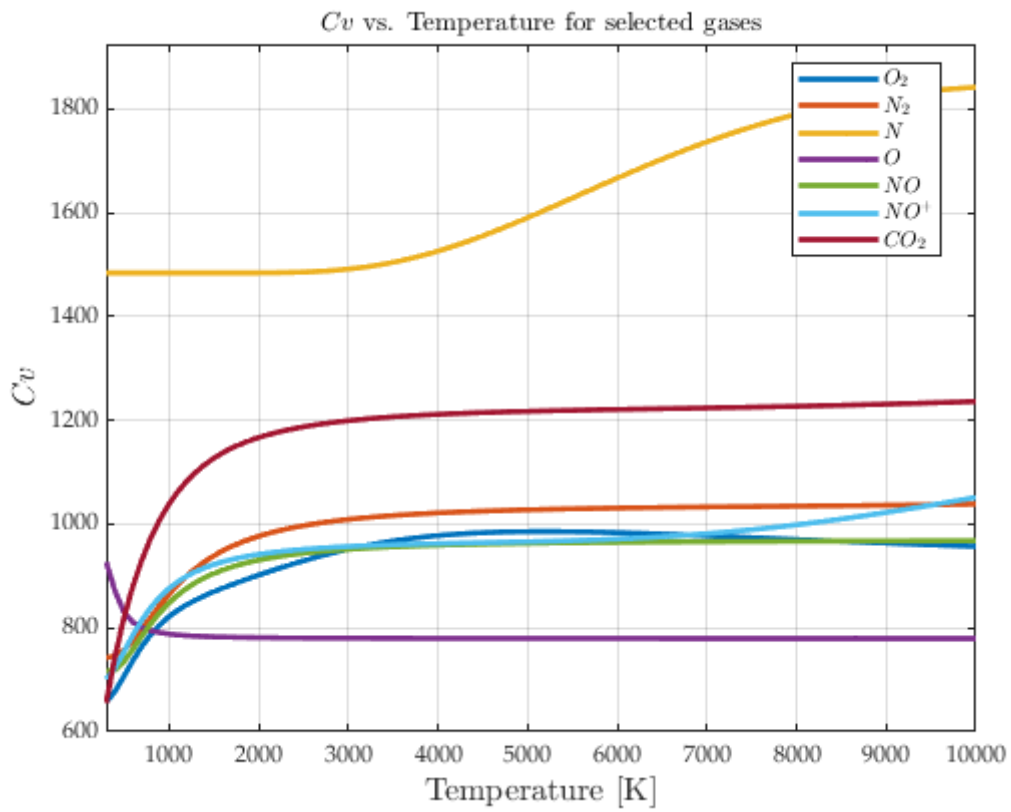


CO2

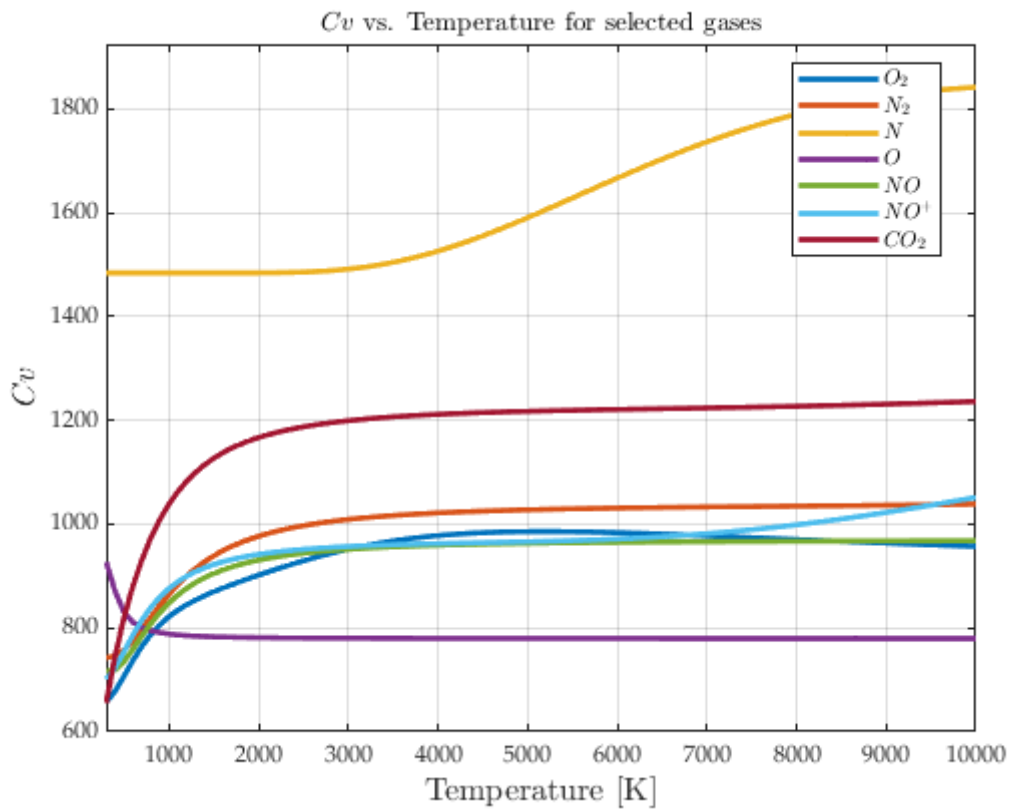


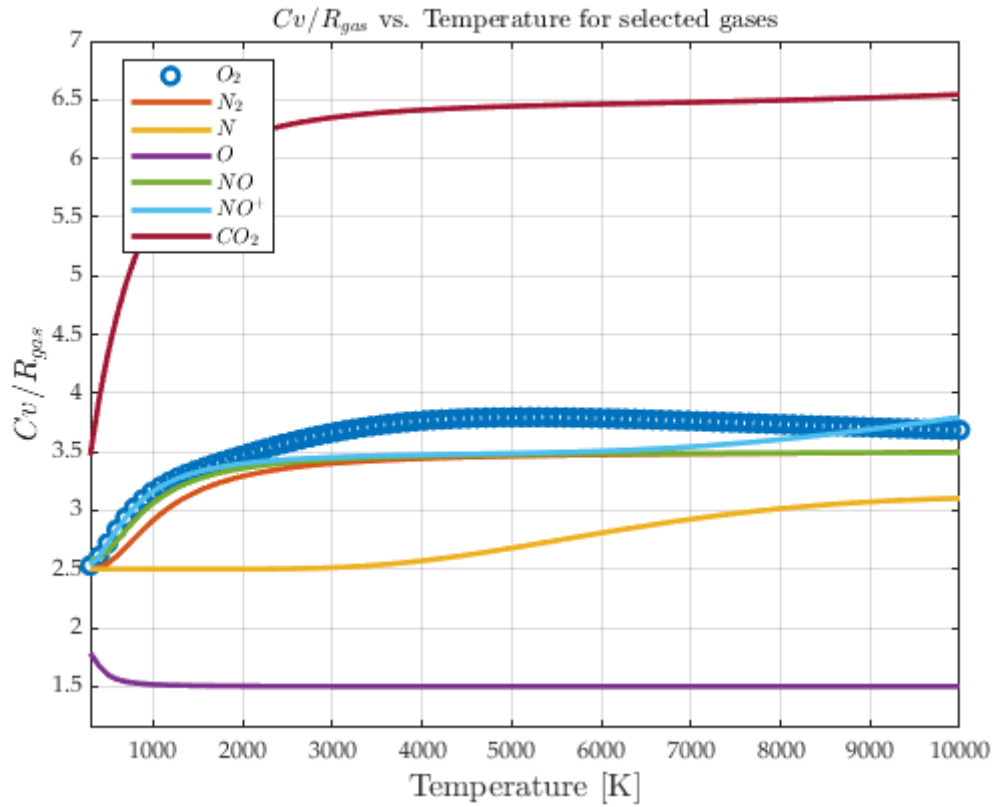


Plot all



Plot C_v/R for all





Kp values (thermal equilibrium coefficients)

Published with MATLAB® R2023b

Appendix B: Chemical Equilibrium Flowchart

